

A Search for Planetary Nebulae With the SDSS: the outer regions of M31⁰

Alexei Y. Kniazev^{1,2,3,4,7}, Eva K. Grebel⁴, Daniel B. Zucker^{5,6}, Hans-Walter Rix⁷, David Martínez-Delgado⁴, Stephanie A. Snedden⁸

akniazev@sao.ac.za

ABSTRACT

We have developed a method to identify planetary nebula (PN) candidates in imaging data of the Sloan Digital Sky Survey (SDSS). This method exploits the SDSS' five-band sampling of emission lines in PN spectra, which results in a color signature distinct from that of other sources. Selection criteria based on this signature can be applied to nearby galaxies in which PNe appear as point sources. We applied these criteria to the whole area of M31 as scanned by the SDSS, selecting 167 PN candidates that are located in the outer regions of M31. The spectra of 80 selected candidates were then observed with the 2.2m telescope at Calar Alto Observatory. These observations and cross-checks with literature data show that our method has a selection rate efficiency of about 90%, but the efficiency is different for the different groups of PNe candidates.

In the outer regions of M31, PNe trace different well-known morphological features like the Northern Spur, the NGC 205 Loop, the G1 Clump, etc. In

⁰ Based in part on observations collected at the German-Spanish Astronomical Center (DSAZ), Calar Alto, operated by the Max-Planck-Institut für Astronomie Heidelberg jointly with the Spanish National Commission for Astronomy

¹South African Astronomical Observatory, PO Box 9, 7935, South Africa

²Southern African Large Telescope Foundation, PO Box 9, 7935, South Africa

³Sternberg Astronomical Institute, Lomonosov Moscow State University, Moscow, Russia

⁴Astronomisches Rechen-Institut, Zentrum für Astronomie der Universität Heidelberg, Mönchhofstr. 12 – 14, D-69120 Heidelberg, Germany

⁵Department of Physics and Astronomy, Macquarie University, NSW 2109, Australia

⁶Australian Astronomical Observatory, P.O. Box 296, Epping, NSW 1710, Australia

⁷Max-Planck-Institut für Astronomie, Königstuhl 17, D-69117 Heidelberg, Germany

⁸Department of Astronomy, New Mexico State University, Box 30001, Las Cruces, NM 880033, USA

general, the distribution of PNe in the outer region $8 < R < 20$ kpc along the minor axis shows the “extended disk” – a rotationally supported low surface brightness structure with an exponential scale length of 3.21 ± 0.14 kpc and a total mass of $\sim 10^{10} M_{\odot}$, which is equivalent to the mass of M33. We report the discovery of three PN candidates with projected locations in the center of Andromeda NE, a very low surface brightness giant stellar structure in the outer halo of M31. Two of the PNe were spectroscopically confirmed as genuine PNe. These two PNe are located at projected distances along the major axis of ~ 48 Kpc and ~ 41 Kpc from the center of M31 and are the most distant PNe in M31 found up to now.

With the new PN data at hand we see the obvious kinematic connection between the continuation of the Giant Stream and the Northern Spur. We suggest that 20 – 30% of the stars in the Northern Spur area may belong to the Giant Stream. In our data we also see a possible kinematic connection between the Giant Stream and PNe in Andromeda NE, suggesting that Andromeda NE could be the core or remnant of the Giant Stream. Using PN data we estimate the total mass of the Giant Stream progenitor to be $\approx 10^9 M_{\odot}$. About 90% of its stars appear to have been lost during the interaction with M31.

Subject headings: galaxies: evolution – galaxies: individual (M31) – galaxies: structure – galaxies: abundances – Local Group

1. Introduction

Planetary nebulae (PNe) arise from intermediate- and low-mass stars, which makes them an excellent probe of the dynamics of these stars in nearby galaxies. Their bright emission lines can provide accurate line-of-sight velocities with a minimum of telescope time. Therefore spectroscopy of PNe can be used as a powerful tool for the study of the kinematics of nearby galaxies (e.g., Hurley-Keller et al. 2004; Peng et al. 2004; Merrett et al. 2006, hereafter HK04, PFF04, and M06) and for the mapping of stellar streams around massive galaxies such as M31 (Merrett et al. 2003; Morrison et al. 2003). The spectra of individual PNe in nearby galaxies also provide chemical abundances of certain elements in their progenitor stars (e.g., Walsh et al. 1997; Richer et al. 1998; Kniazev et al. 2007, 2008; Saviane et al. 2009; Magrini & Gonçalves 2009; Kwitter et al. 2012; Sanders et al. 2012). They complement photometric or spectroscopic metallicity information traditionally derived from old red giants or from H II regions by providing a probe of the abundances of intermediate-age populations.

Searches for PNe are usually based on narrow-band imaging in the $H\alpha$ and $[\text{O III}] \lambda 5007$ bandpasses in which PNe can emit 15–20% of their total luminosity (e.g., Magrini et al. 2003; Magrini et al. 2005a). Occasionally special instruments like the Planetary Nebula Spectrograph (PM.S; Douglas et al. 2002) are employed for the simultaneous identification of PNe and the measurement of their radial velocities (e.g., Merrett et al. 2006), or integral field spectrographs are used in small fields of view with particularly high crowding in order to identify and measure $[\text{O III}] \lambda 5007$ emission against a pronounced stellar background (Pastorello et al. 2013). Other searches, especially photometric ones, aim at covering as large an area as possible.

The Sloan Digital Sky Survey (SDSS) (York et al. 2000; Stoughton et al. 2002) was an imaging and spectroscopic survey that covered about one quarter of the celestial sphere. The imaging data were collected in drift-scan mode in the five bandpasses u , g , r , i , and z (Fukugita et al. 1996; Gunn et al. 1998; Hogg et al. 2001). The images were subsequently processed with special data reduction pipelines to measure the photometric, astrometric, and structural properties of all detectable sources (Lupton et al. 2002; Stoughton et al. 2002; Smith et al. 2002; Pier et al. 2003) and to identify targets for spectroscopy. The SDSS passbands were carefully chosen to provide a wide color baseline, to avoid night sky lines and atmospheric OH bands, to match passbands of photographic surveys, and to guarantee good transformability to existing extragalactic studies.

The SDSS has been used extensively for the detection and characterization of objects with special characteristics, including different types of emission-line objects (e.g., Richards et al. 2002; Kniazev et al. 2003, 2004a; Pustilnik & Tepliakova 2011; Tanaka 2012; Zhao et al. 2013). Since the detected flux from PNe comes almost entirely from nebular emission lines in the optical, the range of colors characteristic of PNe is defined by the ratios of these emission lines and their corresponding contributions in different SDSS passbands. Some of these colors may be expected to be similar to the colors of emission-line galaxies (ELGs; see, e.g., Kniazev et al. 2004a) and should be usable for the detection of PNe based on SDSS photometry.

In this paper, we present a method designed to detect PN candidates based on their SDSS colors. Using a sample of known PNe, we isolate a region in the SDSS $ugri$ two-color diagram in which the probability of an object to be a PN is very high. In §2 we describe the detection method. We apply this method to the M31 region scanned by the SDSS in 2002 (DR6, Adelman-McCarthy et al. 2008). In §3 the follow-up observations and data reduction are described. In §4 we compare our data with other surveys for PNe in M31. In §5 the resulting detection efficiency of the method is discussed. In §6 we present our results for the new PNe in M31 and discuss them. A summary is presented in §7. For the remainder of

this paper, we assume a distance to M31 of 760 kpc (van den Bergh 1999).

2. The Method

2.1. Primary Selection Criteria

In order to develop a method for the selection of PN candidates from Sloan Digital Sky Survey (SDSS) imaging data based on photometric criteria, we used an SDSS scan of M31 reduced with the standard SDSS photometric pipeline (see Zucker et al. 2004a). Using 37 PNe in M31 from Nolthenius & Ford (1987, NF87 hereafter) and one PN from Jacoby & Ford (1986) we constructed a test sample of previously known PNe in this region. We re-identified these PNe in the SDSS data and developed selection criteria on the basis of their SDSS colors and magnitudes. Because the standard SDSS pipeline (PHOTO) does not work properly in very crowded fields, there are *no* SDSS data in the central area of M31 where many of the previously identified PNe in M31 are located. In addition, eight PNe from the list of 37 from Nolthenius & Ford (1987) could not be recovered since they are either located close to diffraction spikes of bright stars on SDSS images or lie in regions where the SDSS source detections are incomplete due to crowding. Our final test sample contained 30 PNe.

The location of the known PNe from our test sample and of other stellar sources from the SDSS M31 data in different color-magnitude diagrams (CMDs) is shown in Figure 1. Throughout this paper, we use magnitudes resulting from point spread function (PSF) fitting in the SDSS photometry pipeline, as these magnitudes give the best results for point sources in the SDSS. To minimize any reddening effects, the measured magnitudes for each object and each filter were corrected using the extinction values from the Schlegel, Finkbeiner, & Douglas (1998) maps prior to further analysis.

One of the basic characteristics for PNe is the magnitude m_{5007} , which is an equivalent of the V-magnitude calculated from the flux of the emission line [O III] $\lambda 5007$ (Jacoby 1989). The SDSS filter g (central wavelength 4686 Å) covers this emission line in a region very close to the maximum of its response. Since PNe at the distance of M31 are objects without detected continuum we assume that the g magnitudes for these objects have to be very close to the m_{5007} magnitudes (see Section 4 for the final comparison). Our final criteria to recover

all objects of the test sample from the SDSS photometric database are:

$$\begin{aligned}
 \text{Object type} &= \text{star} \\
 \text{Magnitude type} &= \text{PSF} \\
 19^{\text{m}}9 &\leq g_0 \leq 21^{\text{m}}6 \\
 (g - r)_0 &\leq -0^{\text{m}}4 \\
 (r - i)_0 &\leq -0^{\text{m}}2 \\
 (u - g)_0 &\geq 1^{\text{m}}0
 \end{aligned} \tag{1}$$

As Figure 1 demonstrates the most important CMD is $(u - g)_0$ versus g_0 , in which the locus of all PNe from our test sample is clearly separated from the location of most other stars in this diagram. The very red $(u - g)_0$ colors of PNe are defined by the existence of strong [O III] $\lambda 5007$ emission in the g filter and the absence of any strong emission lines in the u filter. The limiting magnitude for the bright end of the PN distribution, $g_0 = 19^{\text{m}}9$, was selected on the basis of the distance modulus $(m - M)_0 = 24.4$ to M31 (van den Bergh 1999) and the absolute magnitude cut-off of the PN [O III] $\lambda 5007$ luminosity function (PNLF) in massive galaxies with a large population of PNe ($M_{5007} = -4^{\text{m}}47$; Ciardullo et al. 2002). The limiting magnitude for the faint end and the bluest limiting $(u - g)_0$ color of the PNe was selected such as to recover all objects of the test sample.

The locus of the PNe from the test sample defines the selection parameter range for our “first priority” candidates. Since these are objects whose photometric properties match those of the known PNe from the test sample, they are considered to be very likely PNe as well. However, it is conceivable that “true” PNe are located not only in this region of parameters, but have some spread around it. PNe could have brighter g_0 magnitudes because g is not exactly identical with a narrow-band m_{5007} filter. We also expect PNe with fainter g_0 magnitudes, because the PNLf for M31 has been traced down to 6 mag fainter from its bright cut-off (Merrett et al. 2006). PNe could also have redder $(u - g)_0$ colors in the case that the [O III] $\lambda 5007$ line is not as strong as for objects from the test sample.

For these reasons, based only on the distribution plotted in the $(u - g)_0$ vs. g_0 CMD, we additionally defined more relaxed selection criteria of $19^{\text{m}}4 \leq g_0 \leq 22^{\text{m}}2$ and $(u - g)_0 \geq 0^{\text{m}}6$ to identify “second priority” candidates. We realized that we can assess how good or bad these relaxed criteria are only after getting additional information or confirmation observations for the selected candidates. These softer criteria for the selection of the second priority candidates are indicated with dotted lines in the bottom-right $(u - g)_0$ vs. g_0 diagram in Figure 1. As can be seen from this figure, for magnitudes fainter than $g_0 = 22^{\text{m}}2$, the CMD data become very uncertain because of the incompleteness of the SDSS M31 data themselves. The completeness of the SDSS M31 data varies from field to field because of, for

instance, variable seeing during the observations and photometry pipeline problems caused by crowding. Because of the high stellar density in the M31 region, the incompleteness is higher than in standard SDSS imaging data, which have 95% completeness for point sources at the level of $r \sim 22^m2$ (Abazajian et al. 2004).

We then applied our criteria to the whole area of M31 observed by the SDSS in 2002 (Adelman-McCarthy et al. 2008) in order to select PN candidates. Since the star-galaxy separation in the SDSS is better than 90% at $r = 21^m6$ (Abazajian et al. 2003), but worsens for fainter magnitudes, fainter PNe may have been wrongly identified as (slightly) extended sources in the SDSS database. In our case $r = 21^m6$ can be transformed to $g_0 \sim 20^m6$ using $(g - r)_0 \sim -1$ from Figure 1, and could be even brighter. In order not to lose such potential PNe, we applied the same color and magnitude selection criteria as listed above to extended objects and selected additional PN candidates of first and second priority. Subsequently all candidates were visually inspected to eliminate recognizably false detections, such as diffraction spikes of bright stars and clearly extended objects.

We also visually checked our selected candidates using the images of the “Survey of Local Group Galaxies Currently Forming Stars” (SLGG hereafter; Massey et al. 2006, 2007). In this survey, imaging was obtained in broadband *UBVRI* filters and in narrow-band filters centered on the $H\alpha$ and $[\text{O III}]\lambda 5007$ lines. Using the SLGG we marked those of our candidates with obvious emission in the $[\text{O III}]\lambda 5007$ and $H\alpha$ narrow-band filters and removed all candidates without such emission. This work was done only for that part of our sample covered by the SLGG images.

In the end, we detected a total of 167 PN candidates, 100 first priority and 67 second priority. By design, all PNe from the test sample were detected as candidates of the first priority. We list all selected M31 PN candidates in the SDSS data in Table 1. This table contains the designations (column 1), coordinates (columns 2–3), PSF magnitudes corrected for the extinction and magnitude uncertainties as given by the SDSS (columns 4–8), and the priority type (column 9). The table also shows the result of our spectroscopic follow-up observations and visual checks with data from the SLGG (column 10; see Section 3.1 for detailed explanations), cross-identifications with other catalogs of PNe in M31 (column 12), and the possible association of objects from our sample with some structures of the outer region of M31 (column 11). In Figure 2 we show the positions of all selected candidates of both priorities in our survey using a standard coordinate projection centered on M31.

2.2. Possible Contaminants

In order to understand possible contamination by point sources such as QSOs and stars, we analyzed the distribution of our candidates as compared to the known loci of quasars of different redshifts as shown and discussed in Richards et al. (2002) and Schneider et al. (2010). Our analysis shows that our criteria select star-like sources that are far from both the QSO loci and the loci of the Galactic stars fainter than $g_0 \sim 15.3$ mag. Only a few data points from stars are located in our areas of interest, which would yield perhaps 1–10 objects per 1000 deg². Since the SDSS M31 data studied in this paper cover only about 26 deg² in total (Adelman-McCarthy et al. 2008), including the central part of M31, such contamination should thus be extremely small.

For stars brighter than $g_0 \sim 15.3$ mag foreground stars from the Galaxy begin to contribute as shown in Figure 3, where the CMD for all available stellar sources from the M31 SDSS data is plotted after applying the criteria $(g - r)_0 \leq -0^m4$ and $(r - i)_0 \leq -0^m2$. Figure 3 shows that $g_0 \sim 15.3$ mag is a natural limit of our color-selection method and is far away from the limiting magnitude of 19^m4 we used for the M31 data.

We also estimated the amount of possible contamination by background ELGs using data from Kniazev et al. (2004a) for galaxies with strong emission lines from SDSS Data Release 1 (Abazajian et al. 2003). With our color criteria, only two of the ELGs from the SDSS catalog of Kniazev et al. (2004a) would be selected. These two have very high ([O III] $\lambda 5007/H\beta$) line ratios of 6.5 and 7.2, respectively, which are very close to the characteristics of the PNe from the test sample (see Section 5).

Considering that the above ELG catalog is based on the SDSS Data Release 1, which covers an area of 1360 deg², the number of possible contaminants in our M31 region is obviously very small. Furthermore, the two recovered ELGs are clearly very extended objects and would therefore certainly have been rejected during the visual inspection. These two ELGs are both relatively bright sources with total magnitudes $r \leq 17^m77$ (this was the spectroscopic target magnitude limit for galaxies in the SDSS-I). In contrast, it is conceivable that very distant, very faint ELGs might appear as star-like sources instead. As can be seen in Figure 4, the $(g - r)_0$ color for ELGs increases with redshift. Beyond a redshift of 0.1 all ELGs will lie outside of our color selection area. Hence we may assume that contamination of our PN sample by faint ELGs is negligible.

We conclude that our color-selection method for PN candidates using SDSS *ugri* filters appears to work very well for point-like sources at the distance of M31 with a very low probability for the selected sources to be contaminated with other types of objects. Potentially, this method can work up to the bright limit of $g_0 \sim 15.3$, which corresponds to a distance of

~ 90 kpc (for the absolute magnitude cutoff of the PNLF of $M_{5007} = -4^m47$). For extended sources at the distance of M31, the probability that the selected candidates could be contaminated by nearby (redshift ≤ 0.1) ELGs with strong emission lines is also very low. But this contamination will surely grow when the $(u - g)_0$ color criterion is relaxed (see Section 5 for more details).

3. Spectroscopic Follow-up Observations

3.1. Observations

Spectroscopic follow-up observations of a subset of our PN candidates in M31 were carried out in 2004 October 7 to 14 at Calar Alto Observatory with the Calar Alto Faint Object Spectrograph (CAFOS) at the 2.2 m telescope. During the eight nights of observations in service mode a total of 80 PN candidates of both first and second priorities were observed under variable weather conditions. The seeing varied from $0''.8$ to $2''.5$. A long slit whose width was adjusted depending on the seeing ($1'' - 2.5''$) was used in combination with a G-100 grism (87 \AA mm^{-1} , first order). The spatial scale along the slit was $0''.53 \text{ pixel}^{-1}$. The detector was a SITE $2K \times 2K$ CCD, which we used without binning. The resulting wavelength coverage was $\lambda 4200 - \lambda 6800 \text{ \AA}$ with maximum sensitivity at $\sim 6000 \text{ \AA}$. The obtained dispersion was $\sim 1.9 - 2 \text{ \AA/pixel}$, leading to a spectral resolution of $\sim 4 - 6 \text{ \AA}$ (FWHM). The exposure times were adjusted according to the target brightness and weather conditions and ranged from 15 to 30 minutes per target. In addition, the flux standard star Hiltner 102 was observed at least once per night, and Hg–Cd reference spectra for wavelength calibration were obtained, complemented by the usual dome flatfields, bias, and dark exposures.

We have marked all spectroscopically observed PNe in Table 1. Column 10 specifies which of the PNe were observed at Calar Alto Observatory during our spectroscopic follow-up campaign. Confirmed PNe are marked with the flag value “1”. Three candidates that were not detected as PNe in our follow-up but that were confirmed later via cross-identifications with other catalogues as real PNe are marked with the flag value “2”. PN candidates that were not found in our follow-up observations are marked with the flag value “3”. We did not reject these unconfirmed candidates because all of them are fainter than $g=21^m5$ and possibly were not identified correctly with the 2.2 m telescope under poor weather conditions.

3.2. Data Reduction

The two-dimensional spectra were bias-subtracted and flat-field corrected using IRAF¹. Cosmic ray removal was done with the FILTER/COSMIC task in MIDAS². We used the IRAF software routines IDENTIFY, REIDENTIFY, FITCOORD, and TRANSFORM to perform the wavelength calibration and to correct each frame for distortion and tilt. The accuracy of the velocity determination depends on careful wavelength calibration of the spectra. The rms error in fitting the dispersion curve was always less than 0.3 Å, or 18 km s⁻¹ at a wavelength of 5000 Å. After flux calibration, one-dimensional (1D) spectra were extracted from the reduced frames using the IRAF APALL routine to allow us to measure the total flux. The resulting reduced and extracted spectra of typical observed PNe of different g magnitudes are shown in Figure 5.

After 1D spectra were extracted, we used our standard method for measuring emission-line intensities (Kniazev et al. 2004a, 2005). Briefly, our programs determine the location of the continuum, perform a robust noise estimation, and fit separate emission lines by a single Gaussian superimposed on the continuum-subtracted spectrum. The emission lines H α λ 6563 and [N II] $\lambda\lambda$ 6548,6584 were fitted simultaneously as a blend of three Gaussian features. The quoted uncertainties of the individual line intensities σ_{tot} include two components: σ_p caused by the Poisson statistics of line photon flux, and σ_c , the uncertainty resulting from the creation of the underlying continuum and calculated using the Absolute Median Deviation (AMD) estimator.

Since our data are not of good quality, only the strongest emission lines are detected in our spectra. The emission lines [O III] λ 4959,5007 and H α are seen in all spectra. The emission lines H β and [N II] $\lambda\lambda$ 6548,6584 are detected in most (but not all) spectra. The average signal-to-noise ratios for the detected lines are 33.3 for [O III] λ 5007, 13.2 for H α and 3.8 for H β . Lines with a signal-to-noise ratio less than one were rejected. The strong emission line He II λ 4686 was also found in the spectrum of SDSS J005123+435321, which is located in the area of Andromeda NE (Zucker et al. 2004a) shown in Fig. 5. The observed flux of this line is about 65% of the flux of the H β emission line.

The quoted velocities were derived as mean values weighted by the velocities determined

¹IRAF: the Image Reduction and Analysis Facility is distributed by the National Optical Astronomy Observatory, which is operated by the Association of Universities for Research in Astronomy, Inc. (AURA) under cooperative agreement with the National Science Foundation (NSF).

²MIDAS is an acronym for the European Southern Observatory data reduction package – Munich Image Data Analysis System.

from the individual lines. The weights are inversely proportional to the velocity accuracy for each line. The observed velocities were further corrected for the motion of the Earth and transformed to heliocentric velocities. The resulting radial heliocentric velocities and their errors (column 2), the observed line fluxes (columns 3 – 6), and the derived extinction coefficient $C(\text{H}\beta)$ (column 7) based on the $\text{H}\alpha/\text{H}\beta$ ratio are listed in Table 2. The distributions of the observed $[\text{O III}] \lambda 5007 / \text{H}\alpha$ and $[\text{N II}] \lambda\lambda 6548, 6584 / \text{H}\alpha$ line ratios are shown in Figure 6. The observed and the extinction-corrected $[\text{O III}] \lambda 5007 / \text{H}\alpha$ line ratios are plotted versus the g_0 magnitude in Figure 7.

It is worth noting here that in all cases of non-detection we see no other emission lines in the spectra and do not see any continuum. For this reason we are not able to conclude anything about nature of the candidates that are not identified as genuine PNe: no obvious ELGs, QSOs, or identifiable special types of stars are detected.

4. Comparison with other data sets

After we constructed our sample and obtained follow-up observations, data from four additional surveys for PNe in M31 were published. These new data allow us to compare and to check for different systematic effects or to test the external accuracy. The fifth new survey of the center of M31 (Pastorello et al. 2013) is not included here since the central regions are not resolved in our data.

Hurley-Keller et al. (2004, hereafter HK04) present positions and radial velocities of a sample of 135 PNe, which were selected using narrow-band imaging and follow-up spectroscopy in the area located to the South and East of the nucleus of M31. Halliday et al. (2006, hereafter H06) published positions and velocities for 723 PNe located in the disk and bulge of M31. H06 used the conventional approach of narrow-band imaging and fibre-fed spectroscopy. Merrett et al. (2006, hereafter M06) present a catalogue of positions, magnitudes, and velocities for 3300 emission-line objects (of which 2730 are probably PNe) found by the Planetary Nebula Spectrograph in the area of M31. In our cross-identification work we used a $2.5''$ search box, which is larger than the cited astrometric accuracy of both HK04 and M06.

We did not compare our data with the data of H06, because the M06 sample includes 99% of the H06 sample and the H06 sample is located more in the central region of M31. We also do not compare with the outer disk sample of Kwitter et al. (2012), since their 16 PNe were selected from the M06 data. Finally, we do not compare our data with the survey for PNe in globular clusters in M31 (Jacoby et al. 2013) since due to crowding none of those

PNe and PN candidates are in our sample.

Figure 8 shows the spatial distribution of all PNe from our sample, and of the samples of HK04, H06 and M06 relative to the center and orientation of M31. The PN candidates from our sample are shown with red (first priority) and green (second priority) squares. All observed PNe from our sample that are real PNe are marked by blue squares that are larger in size than the other symbols. All PNe from M06 and H06 are shown with plus signs (+). All PNe from HK are indicated by crosses (x). In this figure, it is easy to see the PNe that belong to both samples (as indicated by square symbols of any color with a cross or plus inside) or that are new ones that were discovered during this work (empty squares).

4.1. Velocities

As was described in Section 2.1 we used PNe from NF87 to define our selection criteria. Therefore the PNe from the NF87 sample are also in our sample. We have nine PNe in common that were re-observed at Calar Alto Observatory. The weighted mean velocity difference $\Delta v(\text{Our} - \text{NF87})$ is $14.3 \pm 6.6 \text{ km s}^{-1}$. This is very close to the systematic difference of 10.4 km s^{-1} that HK04 found comparing their velocities with those of NF87.

In our final sample we have 17 PNe in common with HK04 (six of them are from NF87), but only eight PNe that were re-observed at Calar Alto. The weighted mean velocity difference $\Delta v(\text{Our} - \text{HK04})$ is $3.7 \pm 3.7 \text{ km s}^{-1}$, which means that we do not have any substantial systematic offset in the velocities of our and of the HK04 data. We have 12 PNe in common with H06, seven of which were re-observed at Calar Alto. Similarly, the weighted mean difference $\Delta v(\text{Our} - \text{H06})$ is $1.2 \pm 2.4 \text{ km s}^{-1}$. All these PNe from H06 in our sample are also found by M06.

We have 66 PNe in common with M06 (many of them are in common with NF87 and/or HK04 as well) of which 43 were re-observed at Calar Alto. The weighted mean difference $\Delta v(\text{Our} - \text{M06})$ is $1.6 \pm 3.0 \text{ km s}^{-1}$ with a combined dispersion of 19.5 km s^{-1} , implying that we do not have any systematic offset between our and the M06 data. M06 found that the PN.S data have an uncertainty of 14 km s^{-1} , thus our data have about the same 14 km s^{-1} uncertainty.

4.2. Astrometry and g versus m_{5007}

The PN.S astrometry can also be compared with SDSS astrometry. Both the differences in right ascension (RA) and in declination (Dec) for our 66 PNe in common with M06 are

extremely small ($\Delta\text{RA}(\text{Our}-\text{M06}) = 0.004 \pm 0.9$ arcsec and $\Delta\text{Dec}(\text{Our}-\text{M06}) = 0.08 \pm 0.8$ arcsec) and do not show any systematic effects.

Data from the SDSS together with data from M06 can be used to check our basic hypothesis that the SDSS g magnitudes for PNe are very close to m_{5007} magnitudes. Figure 9 shows a comparison between g magnitudes from the SDSS without extinction correction and m_{5007} magnitudes from M06 for 66 PNe that are common to both samples. As can be seen in the top panel of the figure, most of the points are located around the line of slope unity where both values would equal each other. To check more accurately for possible systematic differences, the value $\Delta(g-m_{5007})$ is drawn in the bottom panel. As this panel shows, the difference does not reveal any systematic trends up to $g \sim 22.5$ mag, which is around our detection limit.

Only five data points show an underestimation of their flux in the PN.S data starting from $m_{5007} \sim 22.0$ mag, or an overestimation of the g magnitude by the SDSS. Since the difference amounts to up to 2.3 mag, but all these PNe were observed with the 2.2m telescope, it seems more likely that the flux was underestimated by M06. Without these five points the g and m_{5007} magnitudes agree within a weighted standard deviation of 0.09 mag, which supports our assumption of the approximate equivalence of the g and m_{5007} magnitudes.

5. The Efficiency of the Method

5.1. Spectral observations

Our spectroscopic follow-up observations of part of our sample allow us to estimate the efficiency of our color-selection method. Altogether, out of the 80 observed PN candidates in the SDSS M31 data, 70 objects turned out to be genuine PNe, resulting in an estimated detection efficiency of $\sim 88\%$. The efficiency is different for the first ($\sim 95\%$) and the second priority ($\sim 63\%$) candidates and depends obviously on the magnitude and color of the selected candidates. The histogram distribution of the PN candidates as a function of magnitude in the g band is shown in Figure 10. Cross-hatched bins indicate observed PN candidates that turned out not to be PNe in our follow-up spectroscopy (no obvious emission lines). As can be seen from this figure the detection efficiency is essentially 100% for magnitudes brighter than $g_0 = 21^{\text{m}}6$, but shows a pronounced decrease for fainter magnitudes.

There are two possibilities inherent to our method and data set that help to explain this trend with luminosity. Firstly, the decreasing number of detected true PNe with decreasing luminosity may reflect the increasing photometric errors for fainter magnitudes and the thus

increasing number of false detections. This affects in particular the SDSS u band, since this band has the lowest sensitivity of all the passbands used in our detection method. At the same time, the incompleteness of true detections is likely to increase towards fainter magnitudes, since especially PNe with weak emission lines may remain unrecognized in the photometric data. Secondly, the small telescope employed for our follow-up observations contributes to the difficulty of confirming fainter candidates. There is at least one PN candidate with $g = 22^m0$, which we re-observed with an exposure time of 1800 s after a 900 s exposure did not reveal emission lines. In the longer exposure emission lines were detected. Furthermore, three additional, known PNe from the lists of HK04 and M06 do not show any emission in our spectra (even though two of them lie within the selection box of our “first priority” objects – see Figure 10). These three PNe are shown in Table 1 with a flag value “2”, and our total efficiency is $\sim 91\%$ ($\sim 98\%$ for the first priority candidates and $\sim 68\%$ for the second) after taking them into account.

Hence we cannot be certain that our faint PN candidates without detected emission lines in their spectra are indeed false identifications – deeper observations or observations with larger telescopes may uncover weak emission lines after all and may thus improve our detection statistics. In this sense, our listed numbers may, in fact, only be lower limits. Therefore we did not remove these candidates from Table 1.

As explained in Section 2.1, very red $(u - g)_0$ colors of PNe are caused by the strong emission line $[\text{O III}] \lambda 5007$ in the wavelength range covered by the g filter and by the absence of any strong emission lines in the u band. The $\text{H}\beta$ emission line is also located in the g filter, close to the position of $[\text{O III}] \lambda 5007$, but the $([\text{O III}] \lambda 5007 / \text{H}\beta)$ line ratio is usually much stronger for spectra of PNe as compared to spectra of ELGs. This contributes to the efficiency of our color-selection method to select PNe as opposed to ELGs.

Using our observational data, we can try to evaluate our $(u - g)_0$ color criterion in terms of this ratio. The distribution of the observed $([\text{O III}] \lambda 5007 / \text{H}\beta)$ line ratio versus the $(u - g)_0$ color is shown in Figure 11. Taking into account that ELGs with strong emission lines have a mean line ratio of 4.06 ± 1.11 (Kniazev et al. 2004a), we can conclude that $(u - g)_0 = 0^m6 - 1^m0$ is approximately the limit where ELGs with strong lines and PNe start to be comparable in SDSS colors.

5.2. Cross-identification with other data

Additional cross identifications with data from HK04 and M06 (73 identifications in total) and visual checks using images of the SLGG (22 identifications in total) provide

further possibilities to evaluate our method. A CMD of the SDSS M31 data with all our PN candidates and those currently known as genuine PNe is shown in Figure 12. All PN candidates are shown as crosses in the selected color-magnitude area. All PNe from the test sample and true PNe confirmed with spectroscopic follow-up observations are shown with red filled circles. All PNe that were identified in the HK04 and/or M06 samples are marked with empty blue circles. All PNe candidates that were not observed or not identified by HK04 and/or M06, but that showed obvious emission in the [O III] $\lambda 5007$ and $H\alpha$ images in the SLGG data are shown with green filled circles. Observed PN candidates without obvious emission lines that are still in the sample are shown as empty red circles. All PNe candidates that were deleted from the sample after the visual inspection of the SLGG data are depicted by empty black circles.

In total, 103 candidates were selected as first priority candidates, out of which three were rejected after checking the SLGG data. Only five first priority candidates still remain to be confirmed. Altogether, this results in an efficiency of our method in the area of the first priority candidates of at least 92%. The efficiency for the area of the second priority candidates drops from $\sim 100\%$ for magnitudes $g < 20^m0$ to $\sim 30\%$ for magnitudes $g > 21^m6$.

Finally, we made one more cross-identification search using the HK04 and M06 sample, but this time for *all* available M31 SDSS data (both stellar and extended sources). We identified only one additional PN as compared to those previously identified in our sample. We thus conclude that with our selection criteria we are able to select 99% of the known PNe in the SDSS M31 data.

We show a comparison of the PNLf from our work with the PNLf from M06 in Figure 13. All data were binned in 0.25 mag intervals. The data were not corrected for reddening. The PNLf from M06 is plotted as a blue line. The black line shows the PNLf for our sample assuming that all selected PN candidates are real PNe. The red line shows the PNLf for confirmed PNe from our sample. As expected for a presumably universal curve regardless of the region sampled, at the bright end our PNLf and the one of M06 show excellent agreement. Our completeness limit is about $g = 21^m0 - 21^m2$.

6. A Few Characteristics of the Planetary Nebulae in M31

6.1. Spatial Distribution

The spatial distribution of all newly discovered PNe is shown in Figure 14. They are overplotted on top of all stars detected by the SDSS. It is obvious that the discovered PNe really trace the distribution of stars in the outer regions of M31. In part, many of them are

seen superimposed on various of the recently uncovered well-known morphological features like the Northern Spur, the NE Shelf, the NGC 205 Loop, the G1 Clump, etc. For a more detailed description of these features and of their stellar populations, see Ferguson et al. (2002, 2005); Ibata et al. (2005, 2007); Richardson et al. (2008).

Certain structures stand out in the spatial distribution of the PNe: A large number of PNe is seen in the area of the Northern Spur and three PN candidates are identified at the location of Andromeda NE (Zucker et al. 2004a). Those newly discovered PNe, which could be associated with known structures in the outer regions of M31, are marked in Table 1. However, whether individual PNe are associated with M31’s disk itself or alternatively with tidal streams (or other M31 components) cannot be decided solely based on their location or spatial coincidence. Such examples will be discussed in the next sections.

There is a certain asymmetry in the distribution of newly detected PNe around M31: we find more in the upper and central portion of Figure 14 (corresponding to the northwestern part of M31) than in the lower portion. Hardly any PNe appear to be associated with the giant stellar stream, while there are several in the area of the NE shelf. Ferguson et al. (2005) point out that the stellar populations of the NE shelf and of the Giant Stream are very similar, but that the Giant Stream is approximately 60 kpc more distant from us than the shelf. Tanaka et al. (2010) found the distance to the Giant Stream to be even twice as large: 883 ± 45 kpc in total. Deeper data might reveal more PNe in these two metal-rich features whose stellar population properties appear to be so similar. Alternatively, the lower number of detected PNe could also be an effect of the PNLFF affected by the inclination of M31’s disk relative to the observer (Merrett et al. 2006), and a higher extinction in the more distant part as seen from our perspective.

6.2. A minor axis density profile for M31

The very extended, diffuse, and disturbed outer regions of M31, which are visible in, e.g., SDSS star counts as shown in Figure 14, is not a unique occurrence. For instance, deep optical surveys of nearby face-on and edge-on dIrrs and disk galaxies have also found that their stellar distributions are much more extended than previously thought, e.g., NGC 6822 (de Blok & Walter 2006), Leo A (Vansevičius et al. 2004), IC 1613 (Battinelli et al. 2007), Pegasus (Kniazev et al. 2009), the Magellanic Clouds (Casetti-Dinescu et al. 2012, and references therein) and the works of Malin & Hadley (1999); Tikhonov (2005, 2006). Moreover, warps and flaring have been shown to be common features of galactic disks (e.g., Gujarro et al. 2010; van der Kruit & Freeman 2011, and references therein). In addition, accretion features are now commonly detected (e.g., Martínez-Delgado et al. 2008, 2009,

2010; Mouhcine et al. 2010; Miskolczi et al. 2011; Ludwig et al. 2012). In the case of M31 we have the opportunity to use PNe as tracers of intermediate-age stellar components in these various structures.

In the case of M31 we appear to see an extension of the disk, which has been shown to possess a complex structure with considerable warping, both in the optical and in H I (e.g., Brinks & Burton 1984; Walterbos & Kennicutt 1988; Braun 1991; Morris et al. 1994; Corbelli et al. 2010), probably caused and modified by interactions (e.g., McConnachie et al. 2009; Richardson et al. 2011; Qu et al. 2011). In recent years the surroundings of M31 have been mapped using deep ground-based photometric surveys of the Andromeda galaxy (Ferguson et al. 2002; Irwin et al. 2005; Ibata et al. 2007; McConnachie et al. 2009) with the wide-field cameras of the Isaac Newton Telescope (INT) and the Canada France Hawaii Telescope (CFHT). Ibata et al. (2005, 2007) presented a surface brightness profile for M31 and concluded that along the minor axis, in the region $0.2^\circ < R < 0.4^\circ$, the classical inner (thin) disk of M31 contributes to the profile, but at $0.5^\circ < R < 1.3^\circ$ the extended disk component becomes dominant.

Since PNe trace the distribution of the underlying intermediate-age stellar populations, we construct a PN density profile for M31 using the catalogue of PNe we compiled from our sample and from the samples of HK04, H06, and M06 (see Section 4). We used the same method as in Kniazev et al. (2009), where the density profile for the outer parts of the Pegasus dIrr was constructed using star counts: PN densities were calculated within elliptical apertures with a fixed aspect ratio. The following assumptions and rules were used during this procedure: (1) We assume that the PNLF of M31 does not vary throughout the entire M31 area. (2) For the central part of M31, i.e., the region inside of the classical disk (within an ellipse with a semimajor axis of two degrees in Figure 8), where the standard SDSS software does not work properly due to crowding, the sample from M06 provides most of the PNe and our data added only very few objects. The aspect ratio for this region was chosen to be the same as for the optical disk. All PNe from the compact elliptical galaxy M32 were excluded. The PN densities were calculated in elliptical apertures with a stepwise axis increase of 0.01 degrees. (3) For all PNe outside of this inner region we first limited the sample to PNe brighter than $g = m_{5007} = 22.5$ mag (see Figure 13). In addition, all PNe from the dwarf elliptical galaxy NGC 205 were excluded. An aspect ratio of 3:5 was used for this region (Ferguson et al. 2002; Irwin et al. 2005; Ibata et al. 2007). PN densities were calculated within elliptical apertures with a step of 0.2 degrees. The PN data cover only part of the studied region and this geometrical incompleteness increases with radius. To correct for this effect, we used an “incompleteness factor” – the ratio between the total area for the elliptical annulus and the actually covered area. This factor is about 1.0 at $0.5^\circ < R < 1.0^\circ$, but increases drastically after that. We included this factor in the error propagation. All

subsequent fitting was done with weights of $w_k = \sigma_k^{-1}$, where σ_k is the uncertainty calculated for each level (Kniazev et al. 2004b).

The final density distribution was normalized such that the surface brightness level at a distance of 0.5° from the center of M31 is ~ 25 mag arcsec $^{-2}$. This normalization was chosen in order to be comparable with the V-band minor-axis surface brightness profile shown in Figure 51 of Ibata et al. (2007). Our calculated density distribution along the minor axis is shown in Figure 15. Data calculated for the central part of M31 are marked by small open circles, and data for the outer part are shown as blue circles. Error bars indicating the uncertainties for each point are also plotted.

Our profile looks very similar to the V-band minor-axis surface brightness profile of Ibata et al. (2007, their Figure 51): in the very center at minor axis radii $R < 0.1^\circ$ we clearly see the bulge. Farther out in the region of $0.1^\circ < R < 0.5^\circ$ the classical inner disk (with bumps caused by spiral arms) contributes to the profile. Then the extended disk becomes dominant, and our profile shows an exponential decline out to the $R = 20$ kpc, where our data, in principle, still trace the extended disk. Fitting the data for the region $8 < R < 20$ kpc, we measure an exponential scale length of 3.21 ± 0.14 kpc, which is quite similar to what was found for the same region by Irwin et al. (2005) and Ibata et al. (2007), who found a scale length of 3.22 ± 0.02 kpc along the minor axis profile using photometric data from the INT Wide Field Camera survey of M31. This structure has a very low central surface brightness at a level of $\mu_0 \sim 23$ mag arcsec $^{-2}$.

Various scenarios for the formation of the extended disk were discussed by Ibata et al. (2005). These authors concluded that the most probable scenario is the formation via accretion of many small subgalactic structures. Peñarrubia, McConnachie & Babul (2006) interpreted the extended disk as a possible result of a single dwarf satellite merger (with a mass of $10^9 - 10^{10} M_\odot$) and suggested that the inner disk would not be strongly affected by such an accretion event (see also Hammer et al. 2010). Magrini et al. (2005b) correlate the number of PNe within four magnitudes of the absolute magnitude of the PNLF bright-end cut-off with the total stellar mass for different galaxies (their Fig. 5). Taking the number of PNe detected in the outer region of M31 into account (~ 200), the fact that most of them belong to the extended disk, and considering the relation derived by Magrini et al. (2005b), we can conclude that the PNe in this area trace a total stellar mass comparable to that of M33 ($\sim 10^{10} M_\odot$) or to the stellar mass estimate inferred for M31’s thick disk component as analyzed by Collins et al. (2011). If we then assume that the abundance distribution for PNe in the extended disk was also similar to the distribution for M33, we would expect a mean oxygen abundance value close to $12 + \log(\text{O}/\text{H}) = 8.2 - 8.4$ dex following Magrini et al. (2009).

Finally, we note that a similar, very extended (up to 40–50 kpc) and rotationally supported disk-like structure was found with PN data in the halo of the nearby peculiar giant elliptical galaxy Centaurus A (Peng et al. 2004).

6.3. Extended disk or rotating spheroid?

A number of studies of the M31 surface brightness profile and of the stellar populations in M31 have suggested that fields as far out as 20 kpc were still dominated by the bulge (e.g. Pritchet & van den Bergh 1994; Durrell, Harris, & Pritchet 2001; Irwin et al. 2005). Deep HST imaging studies of selected minor-axis fields out to 35 kpc suggest that both the spheroid and the giant stellar stream contain, in part, similar (though not identical) intermediate-age populations younger than 10 Gyr and that the spheroid populations are polluted with stars from the progenitor of the stream (e.g., Brown et al. 2006, 2007, 2008). These photometric findings are supported by the spectroscopic studies of red giants along the minor axis by Gilbert et al. (2007) and Fardal et al. (2012).

Altogether, out to 20 kpc from the center of M31 we see the superimposed contributions of stars belonging to M31’s spheroid (bulge and halo components), disk components, and accreted components. In their kinematic study, Collins et al. (2011) identify a dynamically hotter thick disk component in M31 (in addition to the colder classical thin disk and extended disk). Dorman et al. (2012), in another kinematic study based on red giants, find that although the disk components dominate in the inner 20 kpc of M31, the inner spheroid can be traced throughout this region as a rotating, hot component.

HK04 had a sample of 135 PNe that only cover a fraction of M31, but their data include a similar range of minor and major axis distances from the center of M31 as the above studies that are based on red giants. HK04 carried out dynamical modeling and conclude that a standard model for the thin and thick disks and bulge can not reproduce the observed PNe kinematics. They suggest that the majority of the PNe in their sample are probably members of a very extended bulge, which rotates rapidly at large distances and dominates over the halo out to at least 20 kpc. (In the more recent literature this hot rotating component is commonly referred to as “inner spheroid” (see, e.g., Dorman et al. 2012; Fardal et al. 2012).

Ibata et al. (2005) discovered an additional extended disk population and reassessed HK04’s data in the light of this discovery. They concluded HK04’s data may favor the disk interpretation, but could not confirm or exclude whether a rotating spheroid is still needed. Merrett et al. (2006) obtained velocities for a vast number of PNe and found that M31’s extended bulge (or spheroid) component can be traced out to ten effective bulge radii or

approximately 15 kpc. Fardal et al. (2007) conclude that Merrett et al. (2006)’s global PNe kinematics can be best represented as a combination of M31 components plus debris from accreted satellites, including the counterrotating shelf structures.

In their kinematic PN study, Halliday et al. (2006) argue that the substantial drop in the PN velocity dispersion from the center of M31 ($\sim 130 \text{ km s}^{-1}$) out to about 11 kpc ($\sim 50 \text{ km s}^{-1}$) along the major axis does not support the existence of a dynamically hot PN halo, but they, too, find evidence for an extended bulge component akin to HK04. For the PNe belonging to the disk component Halliday et al. (2006) find a rotation velocity of $\sim 140 \text{ km s}^{-1}$. As pointed out by Kwitter et al. (2012), the PN velocity dispersions at large radii and those of the thick disk red giants measured by Collins et al. (2011) are roughly in agreement.

A full dynamical model fit to all PN data is beyond the scope of this paper. But considering the data shown in Figures 8, 14, 15, and 16 we suggest that the domination by an immense rotating spheroid traced by PNe out to $R \sim 20 \text{ kpc}$ along the minor axis looks less probable than the extended disk scenario: (1) The spatial PN distribution follows that of the stars with an aspect ratio close to 3:5 for the outer part of M31. (2) The density profile along the minor axis for the PNe is very similar to the surface brightness profile of M31 for the region $0^\circ < R < 0.5^\circ$ and shows a similar exponential-like profile in the region $0.5^\circ < R < 1.5^\circ$. (3) As also found in the studies mentioned earlier, clearly the bulk of the PNe does not show the signature of a kinematically hot halo where all objects would have random velocities except for the very central part dominated by the bulge population; (4) most PNe (except for those in the very central part) exhibit a distribution indicating that they belong to a component that is rotationally supported.

In Figure 16 we show the velocity distribution of all PNe from HK04, H06, M06, and our sample along the major axis of M31. All shown velocities were corrected for the systemic velocity of M31 of $V_{sys} = -306 \text{ km s}^{-1}$ (Corbelli et al. 2010). This plot shows that the majority of the PNe belongs to the rotationally supported system, where most of our new PNe (blue circles) have velocities systematically shifted to lower values. This may be the expected situation in the case of, for example, a simple model for the velocity of stars on circular orbits around M31 (Ibata et al. 2005). Alternatively, we may be seeing the difference between the kinematics of the inner part of M31 and the extended disk as predicted by Peñarrubia et al. (2006). Which of these scenarios is the more likely one cannot yet be answered with the existing data.

There are also indications for the presence of an intermediate-age population in the halo of M31 that may amount to up to 30% of the stars (Brown et al. 2003). The few PNe that deviate from the rotational signature might be members of the halo of M31 or

of its “extended spheroid” (see discussion of the vast extent of M31 in Worthey et al. 2005; Tanaka et al. 2010). Considering the apparent presence of an intermediate-age population in M31’s halo, PNe should exist there as well, but since the number of PNe strongly depends on the luminosity of the underlying population (e.g., Ciardullo et al. 1989) only a handful of PNe can be expected. However, whether the intermediate-age population is indeed part of the halo is still being debated, especially when considering that M31’s disk may be even more extended than commonly thought, that the existing pencil-beam pointings may be contaminated by stream stars, and that there are apparent large-scale variations in the stellar populations in M31’s outer regions (Durrell et al. 2004; Ferguson et al. 2005; Chapman et al. 2006). We find very few PNe with distances of more than 30 kpc from M31’s center.

6.4. PNe in Andromeda NE

We identified three PN candidates at the location of Andromeda NE (Zucker et al. 2004a). The nature of this diffuse low-surface brightness structure in the outer regions of M31 is still unclear. It may be a very low-mass and low surface-brightness galaxy, a portion of an extended stellar tidal stream, or possibly just turn-off material from the disk of M31. Andromeda NE has an absolute luminosity in the g -band of ~ -11.6 mag and a central surface brightness of only ~ 29 mag arcsec $^{-2}$ (Zucker et al. 2004a).

According to Renzini & Buzzoni (1986) the number of stars n_P in any post-main-sequence phase P can be calculated with the equation $n_P = \eta L_T t_P$, where η is the number of stars per unit luminosity that leave the main sequence per year (between 5×10^{-12} to 2×10^{-11} yr $^{-1}$ L_\odot^{-1}), L_T is the total luminosity of the galaxy ($5 \times 10^6 L_\odot$ for Andromeda NE), and t_P is the duration of the evolutionary phase ($\leq 20,000$ years for PNe). Applying this formula shows that the number of PNe that might be expected in Andromeda NE is 0.5–2. These numbers are in good agreement with the number of PN candidates that we found in this area. Both our 2.2m spectroscopy in this paper and later 3.5m (Calar Alto, Spain) and 6m Russian telescope spectroscopy (Kniazev et al., in preparation) confirm that all these candidates are real PNe, which could be used for kinematical and chemical studies of Andromeda NE. Two of the PNe presented in this work are located at projected distances of ~ 48 kpc and ~ 41 kpc from the center of M31 and are the most distant PNe in M31 found up to now.

Ibata et al. (2005) obtained stellar spectra of presumed M31 disk stars with the Keck DEIMOS multi-object spectrograph. Only one of their DEIMOS fields (16.7×5 arcmin) was located in the area of Andromeda NE. The measured heliocentric velocities for 92 stars in this field show a narrow distribution in the region $V_h = -100$ to -200 km s $^{-1}$. This velocity

distribution peaks at about $V_h = -150 \text{ km s}^{-1}$ (Figure 24 in Ibata et al. 2005) though there may be some contamination from Galactic foreground stars. All our newly found PNe in the area of Andromeda NE have heliocentric velocities in a very narrow velocity range close to $V_h = -150 \text{ km s}^{-1}$, which suggests that Andromeda NE has an average velocity close to that value.

6.5. Could Andromeda NE be the core or a remnant of the Giant Stream?

In Figure 16 we show all PNe identified as a possible continuation of the Giant Stream by Merrett et al. (2003). The Giant Stream was first detected by Ibata et al. (2001) at the southeastern outer part of M31, close to the minor axis, and was photometrically and spectroscopically studied at various locations along the stream by, e.g., McConnachie et al. (2003); Ibata et al. (2004); Guhathakurta et al. (2006). The continuation of this stream in the internal part of M31 is rather uncertain. It is also unknown whether the progenitor of the stream has survived, and if so where it is. For these reasons various possible scenarios have been suggested and studied and different models for the Giant Stream have been calculated (e.g., Merrett et al. 2003; Ferguson et al. 2002; Ibata et al. 2004; Fardal et al. 2006, 2007, 2008).

To constrain the stream’s orbit Fardal et al. (2006) carried out N-body simulations. They find that the PN distribution of Merrett et al. (2003) can be fit well when assuming that it is part of the expected extension of the stream. They also note that it is easy to make the orbit of this stream pass through Andromeda NE but warn that there is no strong evidence that Andromeda NE is indeed part of the stream since it is not visibly connected with it.

In Figure 16, we plot all our PNe as green circles that are located within the same region of (X, V_{los}) parameters as the previously identified PNe that may represent a continuation of the Giant Stream (see Fardal et al. 2006). Three of our PNe were identified before, and our velocities for them are very close to the values of Merrett et al. (2006). Two of our PNe are new. It is easy to see that positions of the two new PNe in Andromeda NE are located along the extension of the line that goes through the “continuation of the Giant Stream” PN sample.

In Figure 17 we also plot positions of all these PNe relative to the center and orientation of M31. All PNe from the “continuation of the Giant Stream” sample show a cone-like structure, beginning close to the southeastern minor axis area, then expanding to northeastern direction and covering the Northern Spur and Andromeda NE area.

Taking into account the results of Fardal et al. (2006) and our own plots, we suggest that the PN data support the notion that Andromeda NE could be a remnant of the Giant Stream. If this suggestion is correct, then there are altogether 24 PNe in this putative stream sample.

Using PN surveys of (other) LG galaxies, Magrini et al. (2005b) infer a relation between the number of PNe and the stellar mass of the intermediate-age population of a galaxy. Applying their relation, we estimate that the Giant Stream progenitor had a mass of $\approx 10^9 M_\odot$ (Magrini et al. 2005b), close to the mass of the NGC 205 dwarf elliptical galaxy. Similarly, using the relation between the number of PNe in a given galaxy and its V -band luminosity derived by Magrini et al. (2003), we estimate a total luminosity $10^8 - 10^{8.5} L_\odot$ for the progenitor of the Giant Stream. Comparing this value to its currently measured luminosity, we suggest that about 90% of its stars have been lost during the interaction with M31. This estimate is very close to the calculated dynamical mass of the Giant Stream progenitor, $M_s \approx 10^9 M_\odot$, from Fardal et al. (2006).

Our estimate of the possible luminosity range of the progenitor is of the order of the luminosities of the dwarf elliptical companions of M31 as well as the Local Group dwarf irregular galaxy IC 10. The estimated lower limits of the metallicity of the PNe in NGC 185 and NGC 205 are $12 + \log(\text{O}/\text{H}) = 8.2$ and 8.6 , respectively (Richer & McCall 1995). For the PNe in NGC 147 Gonçalves et al. (2007) find a mean metallicity of $12 + \log(\text{O}/\text{H}) = 8.06^{+0.09}_{-0.12}$. In IC 10, only one PN metallicity based on a direct measurement of T_{eff} has been published so far, yielding $12 + \log(\text{O}/\text{H}) = 7.96$ (Magrini & Gonçalves 2009). The lower limits estimated for the remaining PNe without direct T_{eff} measurements are higher. We recall that for a given luminosity early-type dwarfs tend to have higher metallicities than late-type dwarfs by up to 0.5 dex (e.g., Richer et al. 1999; Grebel et al. 2003). In any case, regardless of the morphological type of the progenitor, these sparse data on known or estimated PN abundances in dwarf galaxies in the inferred luminosity range of the Giant Stream progenitor suggest that the intermediate-age stellar populations in the progenitor may have had metallicities $12 + \log(\text{O}/\text{H})$ of the order of 8.0 to 8.6 dex.

Finally, we would like to emphasize two findings resulting from our PN analysis: (1) The estimated difference in mass between the Giant Stream progenitor (≈ 20 PNe; $\sim 10^9 M_\odot$) and the extended disk of M31 (≈ 200 PNe; $\sim 10^{10} M_\odot$) is an order of magnitude. For that reason the extended disk cannot be the result of a merger of the Giant Stream progenitor and M31 as a number of models have suggested (e.g., Fardal et al. 2006, 2008). (2) Some part of the Giant Stream progenitor may be spread across the extended disk, but its contribution has to be small compared to the material of the extended disk itself.

6.6. The Giant Stream and the Northern Spur connection

The Northern Spur was first noticed by Walterbos & Kennicutt (1988). This structure is located near the northeastern major axis of M31. The direction of the gaseous warp (e.g., Corbelli et al. 2010) provides strong support for the association of the Northern Spur with a warp in the outer stellar disk. Ferguson et al. (2002) were the first to show that this feature is an excess of stars at the same distance as M31 and that it is about a factor of 1.5–2 times more overdense than the G1 clump. They also suggested that the Northern Spur possibly consists of intermediate-age stars of moderate metallicity, $[\text{Fe}/\text{H}] \geq -0.7$ dex. Analyzing a DEIMOS field (16.7×5 arcmin) in this area Ibata et al. (2005) found that the stellar velocities are similar to the velocities of other fields located in the outer part of M31. Ferguson et al. (2002); Zucker et al. (2004a) and Ibata et al. (2007) suggested that the metallicity of the Northern Spur agrees well with those of many other parts of the extended disk of M31 such as the G1 clump and Andromeda NE. Richardson et al. (2008) analyzed HST data of a number of fields sampling different areas of the outer part of M31 and distinguished two types of fields based on the morphology seen in the color-magnitude diagrams. Their “stream-like” fields resemble the populations found in the Giant Stream, while their “disk-like” fields reveal prominent intermediate-age and recent star formation. The Northern Spur belongs to their “disk-like” fields, just as the G1 Clump and Andromeda NE.

Our data provide further support for the presence of intermediate-age populations, since we found 3–4 PNe in the area of the G1 Clump and 7–10 PNe in the area of the Northern Spur. Our Figures 8 and 14 show the high density of detected PNe in the area of the Northern Spur as compared to the neighboring regions, and Figures 16 and 17 show that three of these PNe are kinematically different and belong to the “continuation of the Giant Stream” sample. In this scenario the progenitor of the Giant Stream passed over, near, or through the Northern Spur area and lost there a sufficiently large part of its mass to account for the PNe. Considering the detected PNe, the total mass of the Northern Spur may be estimated to be $6 \times 10^8 M_{\odot}$, of which 20–30% could have been contributed by the Giant Stream. Since the resulting mixture of populations spread over a sufficiently large area and the resulting range of the metallicities is unknown the detection of such a proposed accreted component would be difficult observationally. However, it would be interesting to compare abundances of different PNe from the Northern Spur area with those from an in-situ population in the same area and with PNe from Andromeda NE.

7. Summary and Conclusions

In this paper we present a method to identify extragalactic PNe based on *ugri* SDSS photometry and results from follow-up studies. Our results and conclusions can be summarized as follows:

1. We have developed a method to identify PN candidates in imaging data of the SDSS using their unique characteristics in *ugri* photometric data. We apply and test this technique using M31 and its large number of PNe. Altogether, we identify 167 PN candidates in the M31 area.

2. We demonstrate that our color-selection method for PN candidates using SDSS *ugri* filters can work very well for point-like sources at distances of 90–800 kpc. The probability for the selected sources to be contaminated with other types of objects is very low. For extended sources the probability that the selected candidates could be contaminated by ELGs with strong emission lines and with redshift ≤ 0.1 is also very low. But this contamination will surely grow when the $(u-g)_0$ color criterion is relaxed: $(u-g)_0 = 0^m6 - 1^m0$ is approximately the limit at which ELGs with strong lines and PNe start to be comparable in SDSS colors.

3. We obtained spectroscopic follow-up observations of 80 PN candidates in the M31 area. These observations, additional cross-identification work with other samples, and visual checks with narrow-band images show that the efficiency of our method is at least 92% for the area of our “first priority” candidates. The efficiency for the area of our “second priority” candidates drops from $\sim 100\%$ for magnitudes of $g < 20^m0$ to $\sim 30\%$ for magnitudes of $g > 21^m6$.

4. In general, the distribution of PNe in the outer region of M31, i.e., $8 < R < 20$ kpc along the minor axis follows the rotationally supported low surface-brightness structure with an exponential scale length of 3.21 ± 0.14 kpc, the so-called extended disk suggested by Worthey et al. (2005). This disk-like component is also visible in photometric data from the Isaac Newton Telescope Wide Field Camera survey of M31 (Ibata et al. 2005, 2007). We estimate the total stellar mass of this structure to be $\sim 10^{10} M_\odot$, which is equivalent of the mass of M33.

5. Our spectroscopy confirms that we have found two new PNe in the area of Andromeda NE (Zucker et al. 2004a), a number consistent with the number of PNe that can be expected in a stellar structure of this low a luminosity ($\sim 5 \times 10^6 L_\odot$). These two PNe are located at projected distances of ~ 46 Kpc and ~ 40 Kpc along the major axis from the center of M31.

6. With the new PN data at hand we see a possible kinematic connection between the Giant Stream and PNe in Andromeda NE suggesting that Andromeda NE could be the core

or remnant of the Giant Stream. Using the PN data we estimate the total mass of the Giant Stream progenitor to be $\approx 10^9 M_\odot$, which would imply that about 90% of stars were lost during the interaction with M31.

6. Our data show an obvious kinematic connection between the continuation of the Giant Stream and the Northern Spur. We suggest that 20 – 30% of stars in the Northern Spur area could belong to the Giant Stream.

The Sloan Digital Sky Survey (SDSS) is a joint project of The University of Chicago, Fermilab, the Institute for Advanced Study, the Japan Participation Group, The Johns Hopkins University, the Max-Planck-Institute for Astronomy (MPIA), the Max-Planck-Institute for Astrophysics (MPA), New Mexico State University, Princeton University, the United States Naval Observatory, and the University of Washington. Apache Point Observatory, site of the SDSS telescopes, is operated by the Astrophysical Research Consortium (ARC).

Funding for the project has been provided by the Alfred P. Sloan Foundation, the SDSS member institutions, the National Aeronautics and Space Administration, the National Science Foundation, the U.S. Department of Energy, the Japanese Monbukagakusho, and the Max Planck Society. The SDSS Web site is <http://www.sdss.org/>.

A.Y.K acknowledges the support from the National Research Foundation (NRF) of South Africa and support from the Collaborative Research Area “The Milky Way System” (SFB 881) of the German Research Foundation (DFG) during his visits to Heidelberg. EKG acknowledges support from the Swiss National Science Foundation through the grants 200021-101924/1 and 200020-105260/1.

REFERENCES

- Abazajian et al. 2003, AJ, 126, 2081
- Abazajian et al. 2004, AJ, 128, 502
- Adelman-McCarthy, J.K. et al. 2008, ApJS, 175, 297
- Battinelli, P., Demers, S., & Artigau, É. 2007, A&A, 466, 875
- Braun, R. 1991, ApJ, 372, 54
- Brown, T. M., Ferguson, H. C., Smith, E., Kimble, R. A., Sweigart, A. V., Renzini, A., Rich, R. M., & VandenBerg, D. A. 2003, ApJ, 592, L17

- Brown, T. M., Smith, E., Ferguson, H. C., et al. 2006, *ApJ*, 652, 323
- Brown, T. M., Smith, E., Ferguson, H. C., et al. 2007, *ApJ*, 658, L95
- Brown, T. M., Beaton, R., Chiba, M., et al. 2008, *ApJ*, 685, L121
- Brinks, E., & Burton, W. B. 1984, *A&A*, 141, 195
- Casetti-Dinescu, D. I., Vieira, K., Girard, T. M., & van Altena, W. F. 2012, *ApJ*, 753, 123
- Corbelli, E., Lorenzoni, S., Walterbos, R., Braun, R., & Thilker, D. 2010, *A&A*, 511, A89
- Chapman, S.C., Ibata, R., Lewis, G., Ferguson, A., Irwin, M., McConnachie, A., & Tanvir, N. 2006, 653, 255
- Ciardullo, R., Jacoby, G. H., Ford, H. C., & Neill, J. D. 1989, *ApJ*, 339, 53
- Ciardullo R., Feldmeier J. J., Jacoby G. H., Kuzio de Naray R., Laychak M. B., Durrell P. R., 2002, *ApJ*, 577, 31
- Collins, M. L. M., Chapman, S. C., Ibata, R. A., et al. 2011, *MNRAS*, 413, 1548
- de Blok, W.J.G., Walter, F. 2006, *AJ*, 131, 343
- Dennefeld, M., Kunth, D. 1981, *AJ*, 86, 989
- Douglas, N. G. et al. 2002, *PASP*, 114, 1234
- Dorman, C. E., Guhathakurta, P., Fardal, M. A., et al. 2012, *ApJ*, 752, 147
- Durrell, P.R., Harris, W.E., Pritchett, C.J. 2001, *AJ*, 121, 2557
- Durrell, P. R., Harris, W. E., & Pritchett, C. J. 2004, *AJ*, 128, 260
- Fardal, M.A., Babul, A., Geehan, J.J., Guhathakurta, P. 2006, *MNRAS*, 366, 1012
- Fardal, M.A., Guhathakurta, P., Babul, A., McConnachie, A.W. 2007, *MNRAS*, 380, 15
- Fardal, M.A., Babul, A., Guhathakurta, P., Gilbert, K.M., Dodge, C. 2007, *ApJ*, 682, L33
- Fardal, M. A., Guhathakurta, P., Gilbert, K. M., et al. 2012, *MNRAS*, 3140
- Ferguson, A. M. N., Irwin, M. J., Ibata, R. A., Lewis, G. F., & Tanvir, N. R. 2002, *AJ*, 124, 1452

- Ferguson, A. M. N., Johnson, R. A., Faria, D. C., Irwin, M. J., Ibata, R. A., Johnston, K. V., Lewis, G. F., & Tanvir, N. R. 2005, *ApJ*, 622, L109
- Fukugita, M., Ichikawa, T., Gunn, J. E., Doi, M., Shimasaku, K., & Schneider, D. P. 1996, *AJ*, 111, 1748
- Gonçalves, D. R., Magrini, L., Leisy, P., & Corradi, R. L. M. 2007, *MNRAS*, 375, 715
- Grebel, E. K., Gallagher, J. S., & Harbeck, D. 2003, *AJ*, 125, 1926
- Gilbert, K. M., Fardal, M., Kalirai, J. S., et al. 2007, *ApJ*, 668, 245
- Gilbert, K. et al. 2009, *ApJ*, 705, 1275
- Guhathakurta, P., et al. 2006, *AJ*, 131, 2497
- Guijarro, A., Peletier, R. F., Battaner, E., et al. 2010, *A&A*, 519, A53
- Gunn, J.E. et al. 1998, *AJ*, 116, 3040
- Halliday, C., et al., 2006, *MNRAS*, 369, 97
- Hammer, F., Yang, Y. B., Wang, J. L., et al. 2010, *ApJ*, 725, 542
- Hogg, D.W., Finkbeiner, D.P., Schlegel, D.J., and Gunn, J.E. 2001, *AJ*, 122, 2129
- Hurley-Keller, D., et al. 2004, *AJ*, 616, 804 (HK04)
- Ibata, R., Irwin, M.J., Ferguson, A.M.N., Lewis, G., Tanvir N., 2001, *Nature*, 412, 49
- Ibata, R., Chapman, S., Ferguson, A., Irwin, M., Lewis, G., & McConnachie, A.W. 2004, *MNRAS*, 351, 117
- Ibata, R., Chapman, S., Ferguson, A., Lewis, G., Irwin, M., & Tanvir, N. 2005, *ApJ*, 634, 287
- Ibata, R., Martin, N.F., Irwin, M., Chapman, S., Ferguson, A., Lewis, G., & McConnachie, A. 2007, *ApJ*, 671, 1591
- Irwin, M., Ferguson, A., Ibata, R., Lewis, G., & Tanvir, N. 2005, *ApJ*, 628, L105
- Jacoby, G.H. 1989, *ApJ*, 339, 39
- Jacoby, G. H., & Lesser, M. P. 1981, *AJ*, 86, 185
- Jacoby, G.H., & Ford, H.C. 1986, *ApJ*, 304, 490

- Jacoby, G. H., Ciardullo, R., De Marco, O., Lee, M. G., Herrmann, K. A., Hwang, H. S., Kaplan, E., & Davies, J. E. 2013, *ApJ*, 769, 10
- Lupton, R. H., Ivezić, Z., Gunn, J. E., Knapp, G., Strauss, M. A., & Yasuda, N. 2002, *Proc. SPIE*, 4836, 350
- Kent, S.M. 1989, *AJ*, 97, 1614
- Kniazev, A.Y., Grebel, E.K., Hao, L., Strauss, M.A., Brinkmann, J., & Fukugita, M. 2003, *ApJ*, 593, L73
- Kniazev, A.Y., Pustilnik, S.A., Grebel, E.K., Lee, H., & Pramskij, A.G. 2004a, *ApJS*, 153, 429
- Kniazev A.Y., Grebel E.K., Pustilnik S.A., Pramskij A.G., Kniazeva T.F., Prada F., Harbeck D. 2004b, *AJ*, 127, 704
- Kniazev, A.Y., Grebel, E.K., Pustilnik, S.A., Pramskij, A.G., & Zucker, D. 2005, *AJ*, 130, 1558
- Kniazev, A.Y., Grebel, E.K., Pustilnik, S.A., & Pramskij, A.G. 2007, *A&A*, 468, 121
- Kniazev, A.Y., Zijlstra, A.A., Grebel, E.K., et al. 2008, *MNRAS*, 388, 1667
- Kniazev, A.Y., Brosch, N., Hoffman, G.L., Grebel, E.K., Zucker, D.B., Pustilnik, S.A. 2009, *MNRAS*, 400, 2054
- Kunth, D., & Östlin, G. 2000, *A&A Rev.*, 10, 1
- Kwitter, K. B., Lehman, E. M. M., Balick, B., & Henry, R. B. C. 2012, *ApJ*, 753, 12
- Ludwig, J., Pasquali, A., Grebel, E. K., & Gallagher, J. S., III 2012, *AJ*, 144, 190
- Magrini, L., et al. 2003, *A&A*, 407, 51
- Magrini, L., et al. 2005a, *A&A*, 443, 115
- Magrini, L., et al. 2005b, *MNRAS*, 361, 517
- Magrini, L., Gonçalves, D. 2009a, *MNRAS*, 398, 280
- Magrini, L., Stanghellini, L., & Villaver, E. 2009b, *ApJ*, 696, 729
- Malin, D., & Hadley, B. 1999, in *Galaxy Dynamics – A Rutgers Symposium*, ASP Conf. Ser. 182, eds. D. R. Merritt, M. Valluri, & J. A. Sellwood (ASP: San Francisco), 445

- Martínez-Delgado, D., Peñarrubia, J., Gabany, R. J., Trujillo, I., Majewski, S. R., & Pohlen, M. 2008, *ApJ*, 689, 184
- Martínez-Delgado, D., Pohlen, M., Gabany, R. J., Majewski, S. R., Peñarrubia, J., & Palma, C. 2009, *ApJ*, 692, 955
- Martínez-Delgado, D., et al. 2010, *AJ*, 140, 962
- Massey, P., Olsen, K. A. G., Hodge, P. W., Strong, S., Jacoby, G. H., Schlingman, W., Smith, R. C., 2006 *AJ*, 131, 2478
- Massey, P., McNeill, R. T., Olsen, K. A. G., Hodge, P. W., Blaha, C., Jacoby, G. H., Smith, R. C., Strong, S. B. 2007, *AJ*, 134, 2474
- McConnachie, A. W., Irwin, M. J., Ibata, R. A., et al. 2009, *Nature*, 461, 66
- Merrett, H.R. et al. 2003, *MNRAS*, 346, L62
- Merrett, H.R. et al. 2006, *MNRAS*, 369, 120 (M06)
- McConnachie, A.W., Irwin, M.J., Ibata, R.A., Ferguson, A.M.N., Lewis, G.F., Tanvir, N. 2003, *MNRAS*, 343, 1335
- Miskolczi, A., Bomans, D. J., & Dettmar, R.-J. 2011, *A&A*, 536, A66
- Morris, P. W., Reid, I. N., Griffiths, W. K., & Penny, A. J. 1994, *MNRAS*, 271, 852
- Morrison, H. L., Harding, P., Hurley-Keller, D., & Jacoby, G. 2003, *ApJ*, 596, L183
- Mouhcine, M., Ibata, R., & Rejkuba, M. 2010, *ApJ*, 714, L12
- Nolthenius, R., & Ford, H.C. 1987, *ApJ*, 317, 62 (NF87)
- Pastorello, N., et al. 2013, *MNRAS*, 430, 1219
- Peñarrubia, J., McConnachie, A., & Babul, A. 2006, *ApJ*, 650, L33
- Peng, E.W., Ford, H.C., & Freeman, K.C. 2004, *ApJ*, 602, 685
- Pier, J.R., Munn, J.A., Hindsley, R.B, Hennessy, G.S., Kent, S.M., Lupton, R.H., & Ivezić, Z. 2003, *AJ*, 125, 1559
- Pustilnik, S.A., Tepliakova, A.L. 2011, *MNRAS*, 415, 1188
- Pritchett, C.J. & van den Bergh, S. 1994, *AJ*, 107, 1730

- Qu, Y., Di Matteo, P., Lehnert, M. D., van Driel, W., & Jog, C. J. 2011, *A&A*, 535, A5
- Renzini, A., & Buzzoni, A. 1986, in *Spectral Evolution of Galaxies*, *Astrophysics Space Science Library* 122, eds. C. Chiosi, & A. Renzini (Dordrecht: Reidel), 195
- Richards, G.T. et al. 2002, *AJ*, 123, 2945
- Richardson, J.C. et al. 2008, *AJ*, 135, 1998
- Richardson, J. C., Irwin, M. J., McConnachie, A. W., et al. 2011, *ApJ*, 732, 76
- Richer, M. G., & McCall, M. L. 1995, *ApJ*, 445, 642
- Richer, M., McCall, M. L., & Stasinska, G. 1998, *A&A*, 340, 67
- Richer, M. G., Stasińska, G., & McCall, M. L. 1999, *A&AS*, 135, 203
- Sanders, N. E., Caldwell, N., McDowell, J., & Harding, P. 2012, *ApJ*, 758, 133
- Saviane I., Exter K., Tsamis Y., Gallart C., Péquignot D. 2009, *A&A*, 494, 515
- Schlegel, D., Finkbeiner, D., & Douglas, M. 1998, *ApJ*, 500, 525
- Schneider, D.P. et al. 2010, *AJ*, 139, 2360
- Smith, J.A. et al. 2002, *AJ*, 123, 2121
- Stoughton, C. et al. 2002, *AJ*, 123, 485
- Tanaka, M., Chiba, M., Komiyama, Y., et al. 2010, *ApJ*, 708, 1168
- Tanaka, M. 2012, *PASJ*, 64, 37
- Tikhonov, N.A., 2005, *Astronomy Reports*, 49, 501
- Tikhonov, N.A., 2006, *Astronomy Reports*, 50, 517
- van den Bergh, S. 1999, *A&A Rev.*, 9, 273
- van der Kruit, P. C., & Freeman, K. C. 2011, *ARA&A*, 49, 301
- Vansevičius V., et al. 2004, *ApJ*, 611, L93
- Walsh, J.R., Dudziak, G., Minniti, D., & Zijlstra, A.A. 1997, *ApJ*, 487, 651
- Walterbos, R. A. M., & Kennicutt, R. C. 1988, *A&A*, 198, 61

- Worthey, G., España, A., MacArthur, L. A., & Courteau, S. 2005, ApJ, 631, 820
- York, D.G. et al. 2000, AJ, 120, 1579
- Zhao, J. K., Oswalt, T. D., Zhao, G., Lu, Q.H., Luo, A.L., & Zhang, L.Y. 2013, AJ, 145, 140
- Zucker, D.B., et al. 2004a, ApJ, 612, L117
- Zucker, D. B., et al. 2004b, ApJ, 612, L121

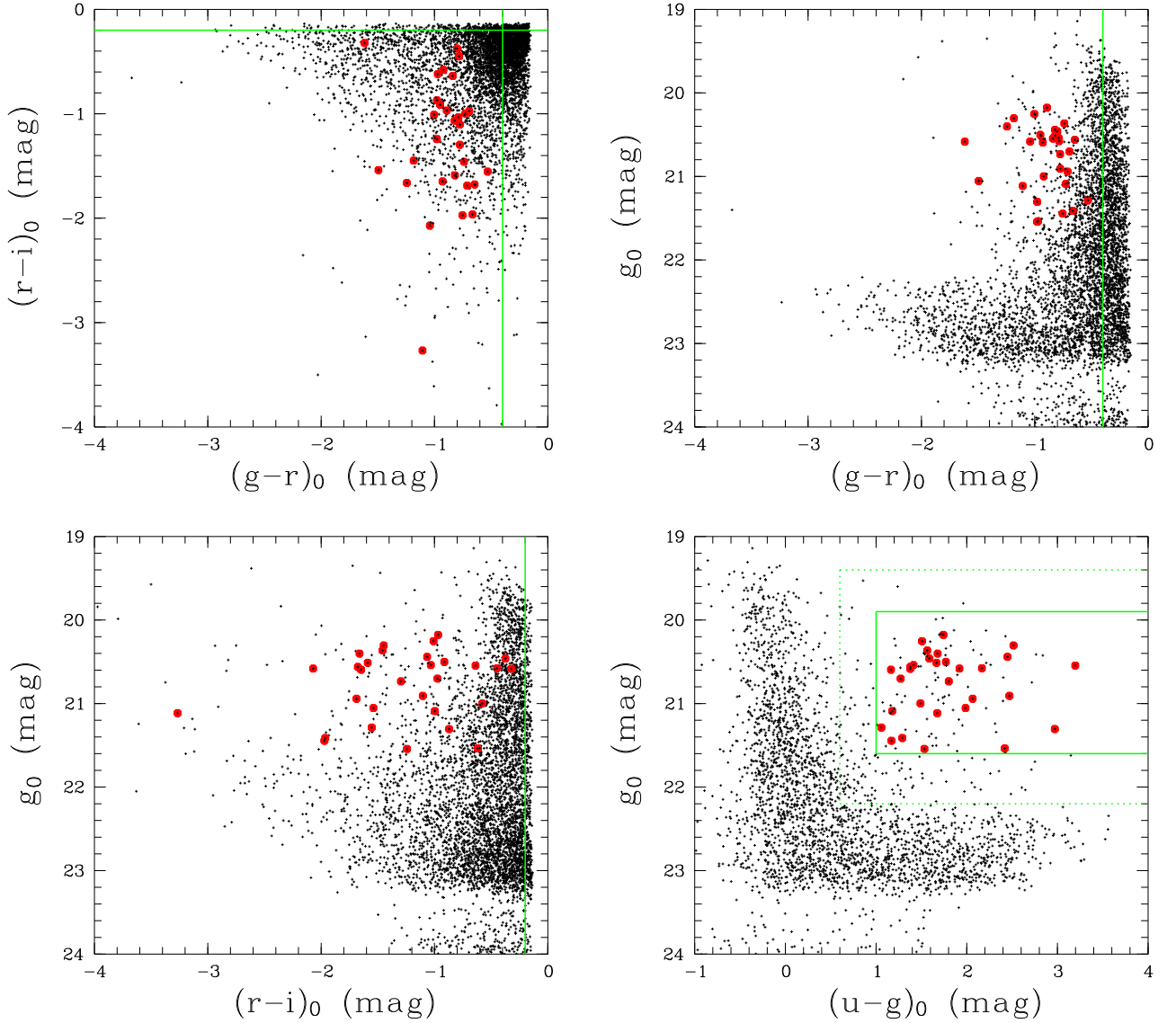


Fig. 1.— Color-magnitude diagrams for sources from SDSS M31 data to which we applied our selection procedure. All previously known re-identified PNe from Nolthenius & Ford (1987) and Jacoby & Ford (1986) are shown with red filled circles. Their locus defines our “first priority” candidates. Our color-magnitude criteria for selecting these candidates are shown by solid lines. Additional dotted lines in the bottom-right g_0 vs. $(u - g)_0$ diagram show softer criteria for the selection of the “second priority” candidates. Within these lines only sources remaining after visual verification are plotted (see Section 2.1 for more details).

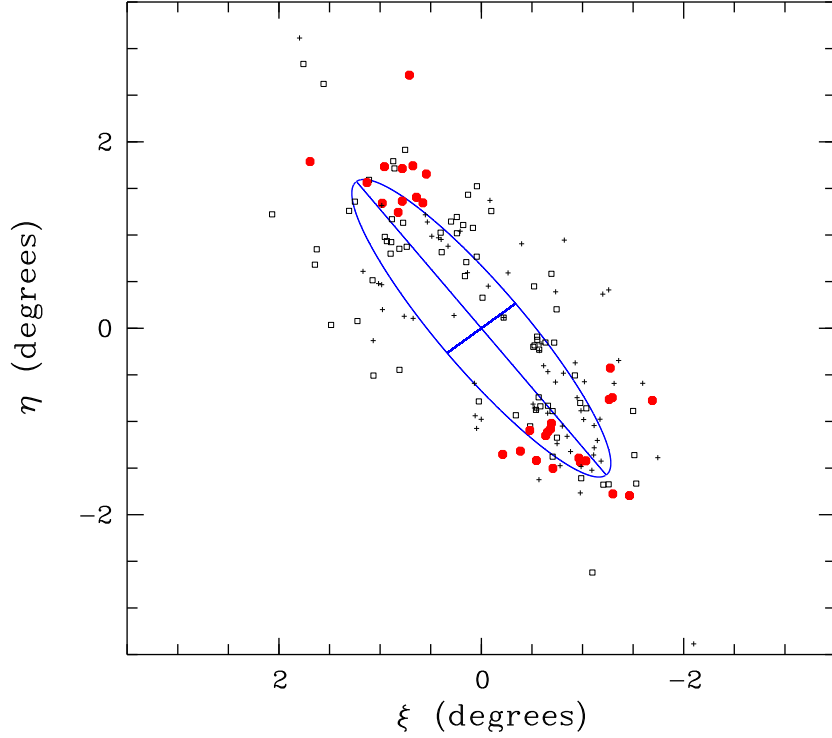


Fig. 2.— Positions of selected candidates relative to the center and orientation of M31. The ellipse has a semimajor axis of 2 degrees (≈ 27 kpc) and represents an inclined disk with $i = 77.5$. The optical disk of M31 lies well within this boundary (Ferguson et al. 2002). First priority candidates are marked with squares and second priority candidates with crosses. PNe from Nolthenius & Ford (1987) and Jacoby & Ford (1986) are shown with filled (red) squares. Three PN candidates are located in the area of Andromeda NE (Zucker et al. 2004a) in the range of the coordinates (2.0–2.5, 2.5–3.0).

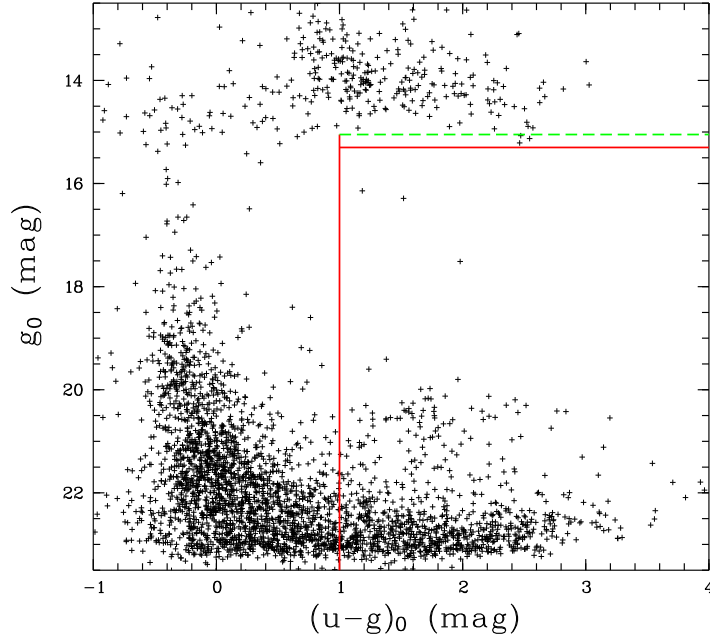


Fig. 3.— Color-magnitude diagram for all stellar sources from SDSS M31 data selected with the criterion $(g-r)_0 \leq -0^m4$ & $(r-i)_0 \leq -0^m2$. Our color-magnitude criterion $(u-g)_0 \geq 1^m0$ for the selection of the first priority candidates is shown with a vertical line. Foreground stars from the Galaxy are located in the region brighter than $g_0 = 15^m3$ that is shown with a horizontal solid line. The magnitude $g_0 = 15^m05$, which corresponds to a distance of ~ 80 kpc for an absolute magnitude cutoff of the PNLf, $M_{5007} = -4^m47$, is shown with a horizontal dashed line. Three star-like sources with g -band magnitudes between 16^m0 and 19^m0 and $(u-g) > 1^m0$ are false detections in the areas around bright saturated stars.

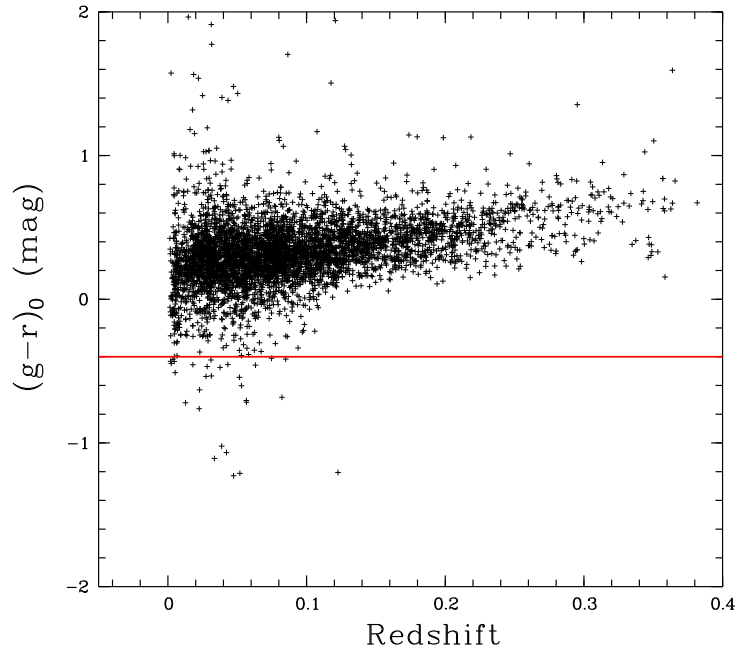


Fig. 4.— The distributions of $(g-r)_0$ colors from PSF photometry for ELGs from Kniazev et al. (2005) versus redshift. Our selection criterion for the $(g-r)_0$ color is shown with a solid red line.

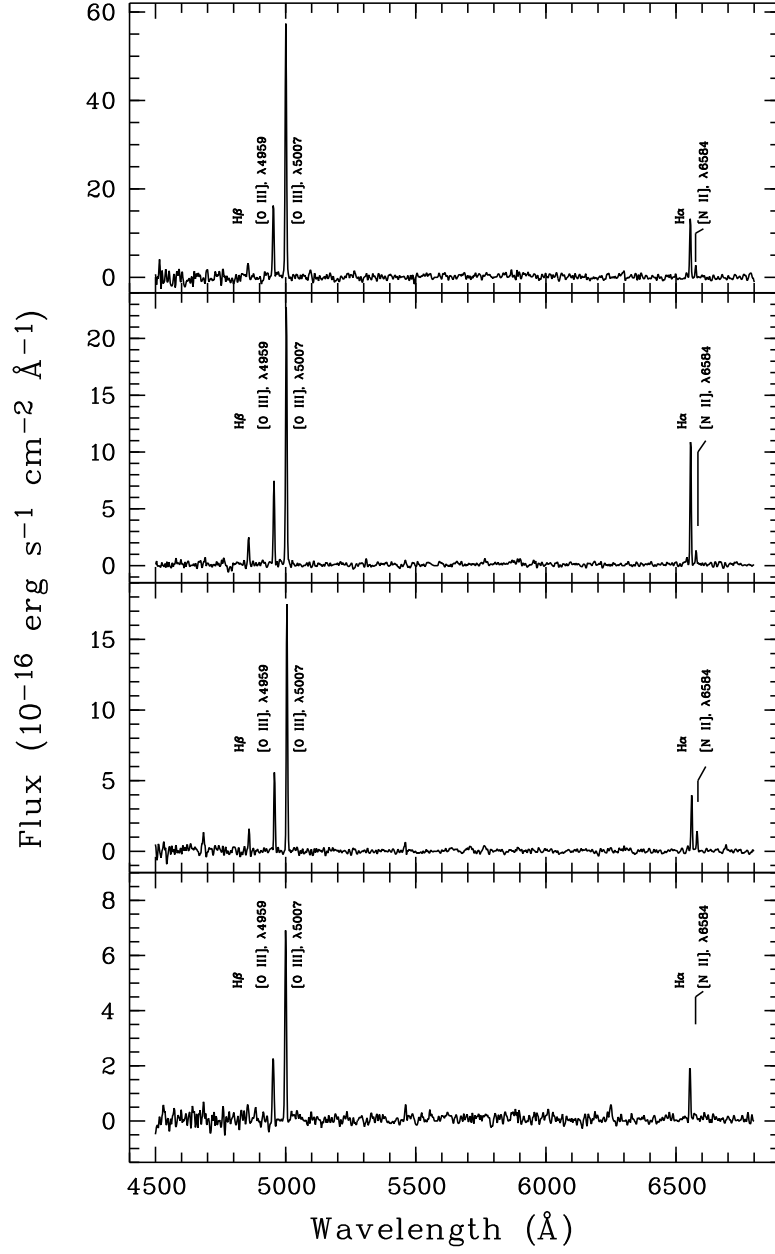


Fig. 5.— Four typical spectra for our sample with different signal-to-noise ratios and g magnitudes ranging from ~ 20 to 21^m6 . All spectra show the strongest emission lines $[\text{OIII}] \lambda 4959, 5007$ and $\text{H}\alpha$.

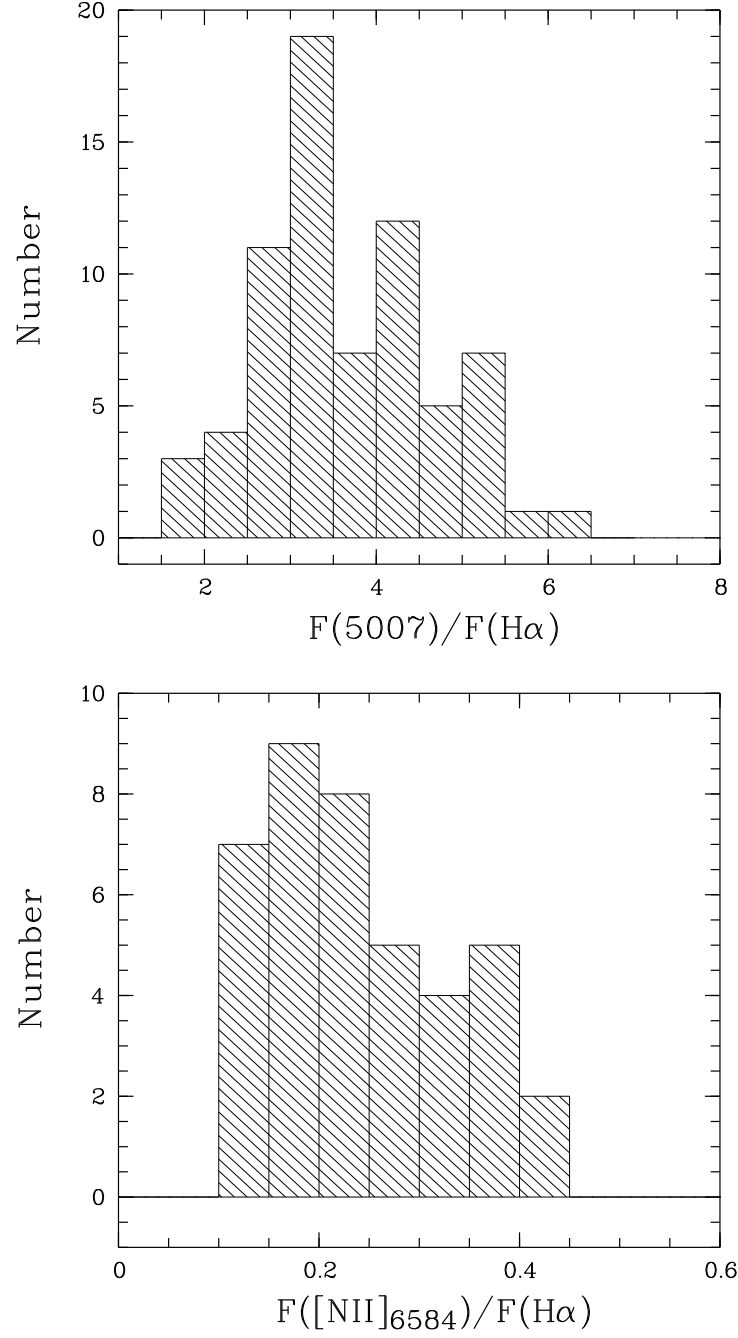


Fig. 6.— Observed line ratios for PNe from our sample. *Top*: The $[O\text{ III}]$ $\lambda 5007$ to $H\alpha$ line ratio. *Bottom*: The $[N\text{ II}]$ $\lambda 6584$ to $H\alpha$ line ratio.

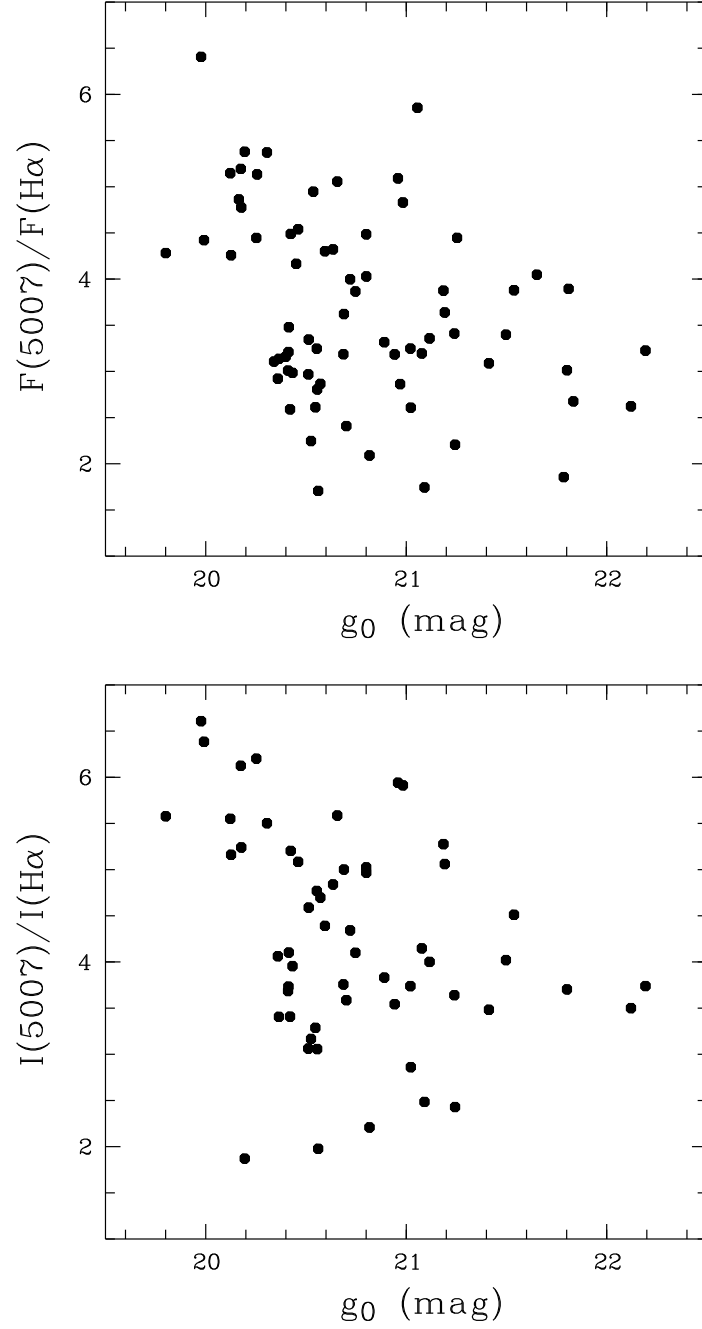


Fig. 7.— *Top*: Observed [O III] $\lambda 5007$ to $H\alpha$ line ratio versus g_0 magnitude. *Bottom*: [O III] $\lambda 5007$ to $H\alpha$ line ratio versus g_0 magnitude after correction for the calculated extinction.

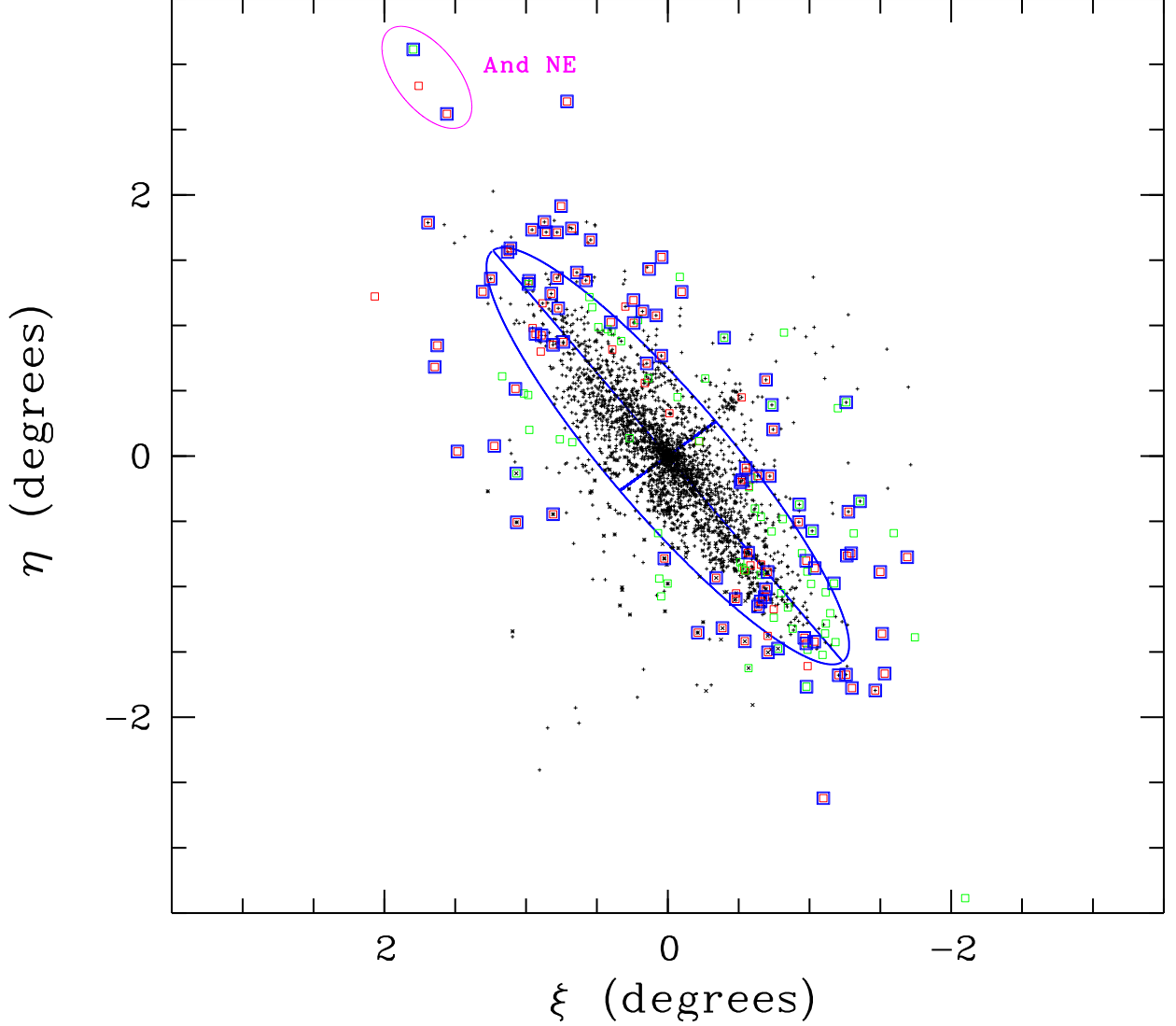


Fig. 8.— Positions of all PNe from the HK, H06, and M06 samples and selected candidates from our work relative to the center and orientation of M31. The PNe from M06 and H06 are shown with plus signs (+). The PNe from HK are shown with crosses (x). First priority candidates from our sample are drawn with red squares and second priority candidates are drawn with green squares. All PNe from the test sample and all observed PNe from our sample that were identified as real PNe are shown with larger blue squares. Two of three PN candidates in the area of Andromeda NE were observed and both of them were confirmed to be real PNe.

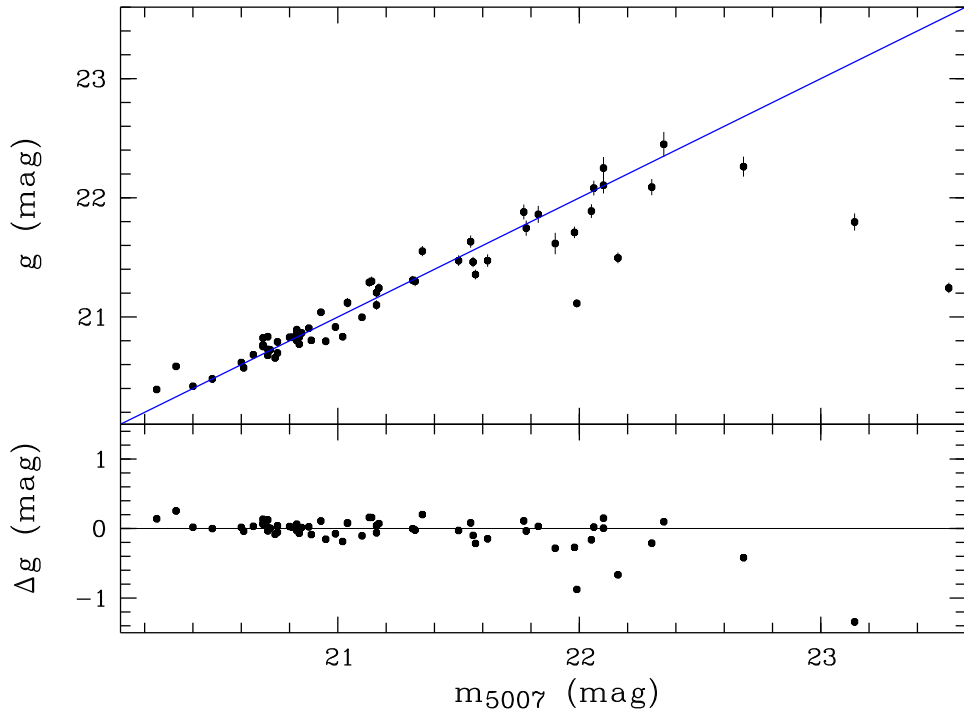


Fig. 9.— Comparison of g magnitudes and m_{5007} magnitudes from M06. *Top*: The solid line represents a line of slope unity where the g magnitudes equal the m_{5007} magnitudes. *Bottom*: Difference between g and m_{5007} magnitudes.

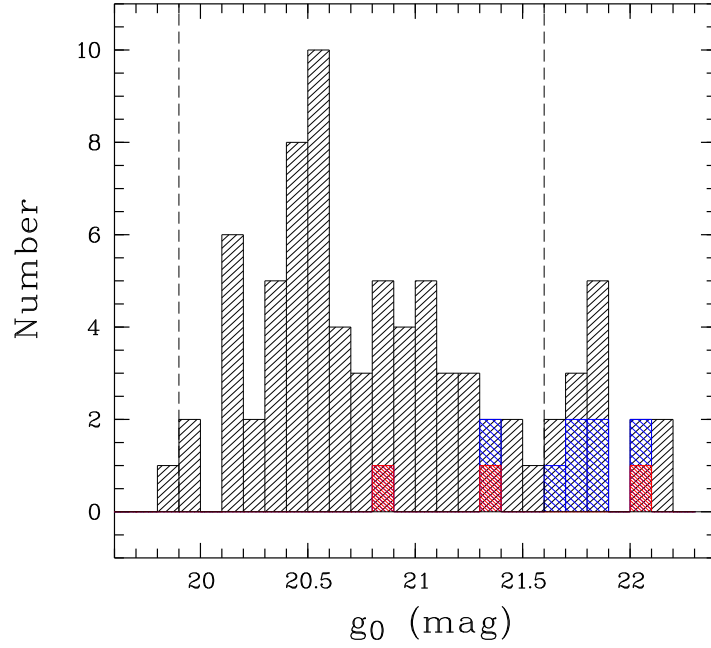


Fig. 10.— Distribution of observed PN candidates in the g_0 band. Blue double hashed bins indicate the distribution of observed PN candidates without obvious emission lines. Red double hashed bins indicate positions of three candidates that were additionally identified as genuine PNe during cross-identification work. The data are binned into 0.1 mag intervals. The magnitude criteria for the second priority candidates selection are shown with vertical lines.

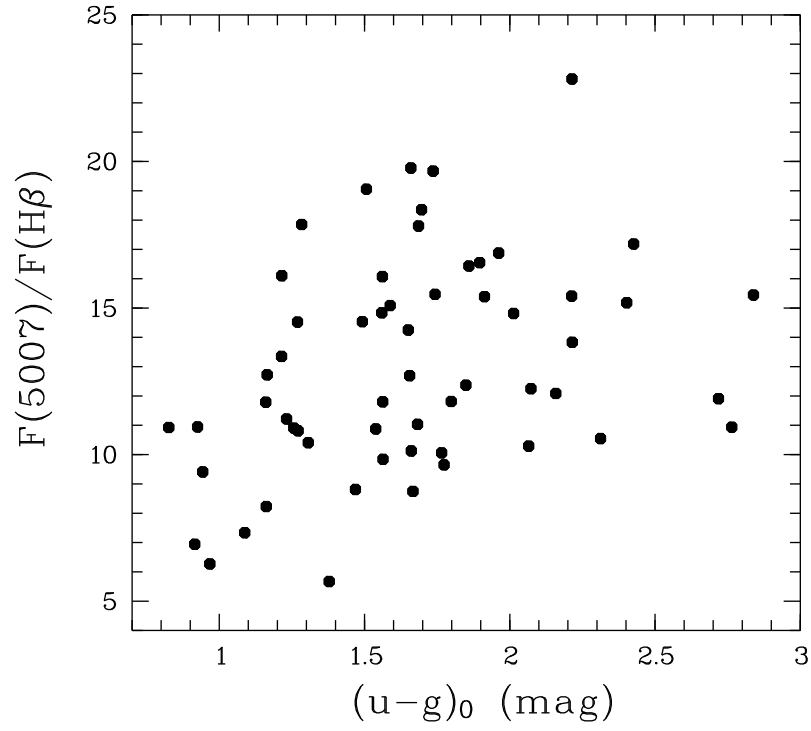


Fig. 11.— Distribution of observed $[\text{O III}] \lambda 5007/\text{H}\beta$ line ratio versus $(u - g)_0$ color to illustrate the working area of our color-selection method.

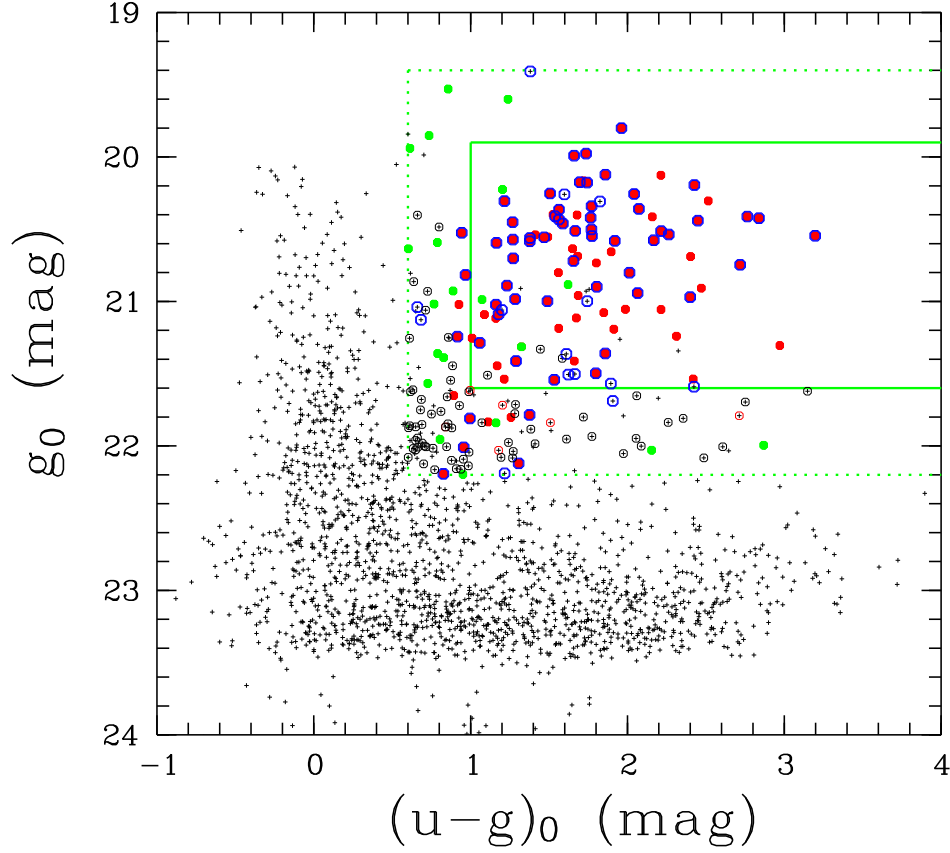


Fig. 12.— Same as the right bottom panel of Fig. 1, but results of observations, cross-identifications with samples from HK04 and M06 and visual checks using images of SLGG are also shown: (1) all PN candidates are shown as crosses in the selected color-magnitude area; (2) all PNe from the test sample and true PNe confirmed with spectroscopic follow-up observations are shown as filled red circles; (3) all observed PN candidates without obvious emission lines are shown with empty red circles; (4) all PNe that also were identified in the HK04 and/or M06 samples are shown with empty blue circles; (5) all non-observed PN candidates that were not identified in the HK04 and/or M06 samples, but that showed obvious emission in $[\text{O III}] \lambda 5007$ and $\text{H}\alpha$ images in the SLGG data are shown with green filled circles; (6) all PN candidates that were deleted from the sample after a cross-check with the SLGG data are shown with empty black circles.

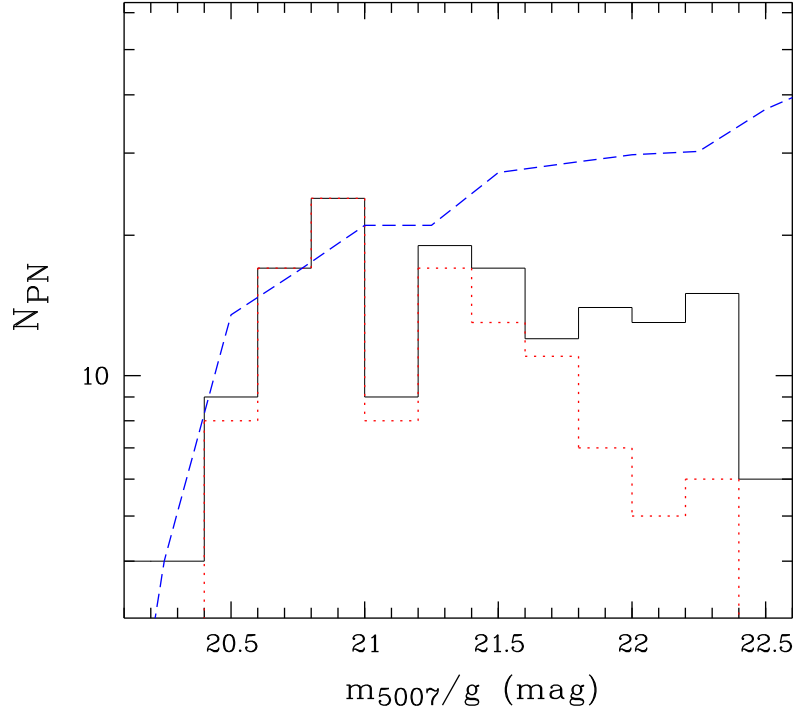


Fig. 13.— Comparison of the PN luminosity function (PNLF) from M06 with the PNLF from this work. The PNLF from M06 (m_{5007} magnitudes) is shown with the blue short dash line. The PNLF based on all our selected candidates (g magnitudes) is shown with the black solid line. The PNLF for all currently known genuine PNe from our sample is shown with the red dotted line. All data were binned into 0.25 mag intervals.

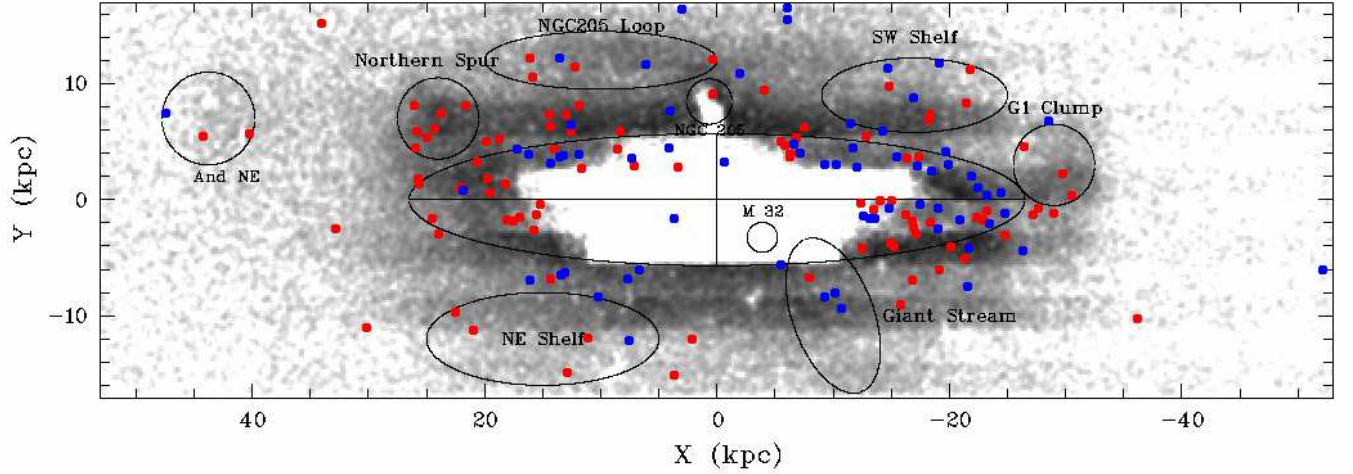


Fig. 14.— Spatial distribution of newly-discovered PNe from the M31 SDSS data. The spatial distribution of all stars that were detected by the SDSS standard pipeline in M31 data is shown. The data were binned by $2' \times 2'$. X and Y are in kpc from the center of M31 along the major and minor axes, respectively. The central ellipse has a semimajor axis of 2 degrees (≈ 27 kpc) and represents the optical disk of M31 with $i = 77.5$, which lies well within this boundary. First priority candidates are shown with red filled circles and second priority candidates are shown with blue filled circles. The other ellipses mark the locations of NGC 205, M32, Andromeda NE, and some other major substructures shown by Ferguson et al. (2002, 2005); Ibata et al. (2007); Richardson et al. (2008).

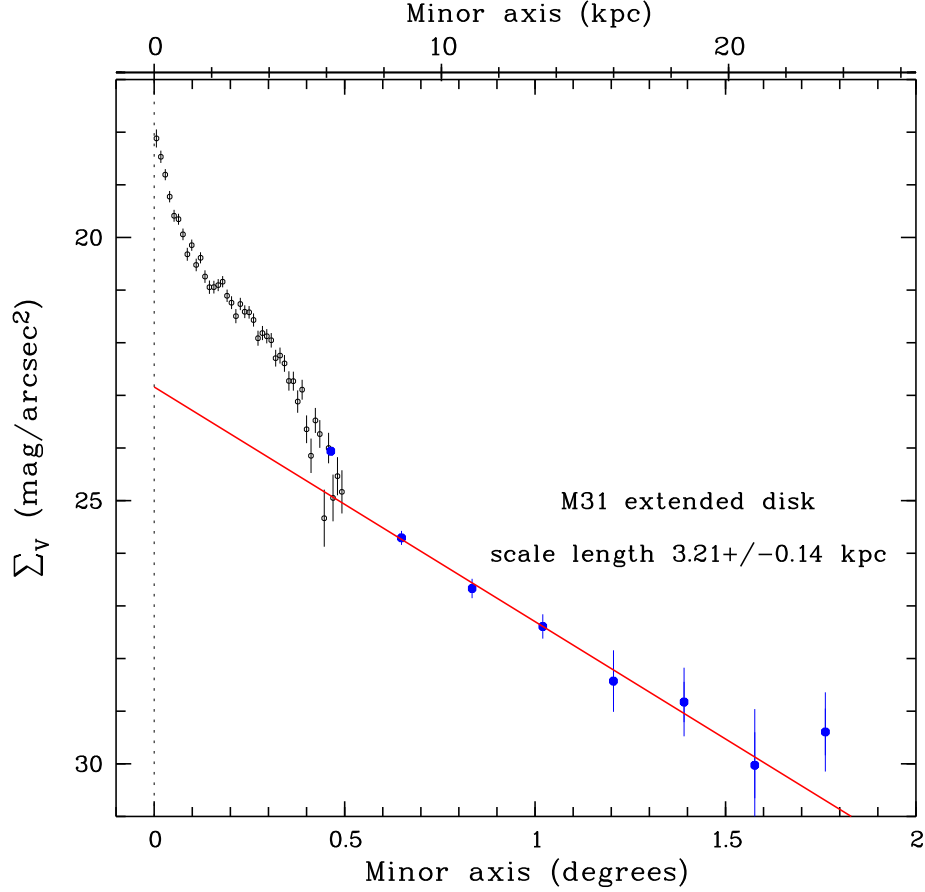


Fig. 15.— Calculated distribution of the PN density along the minor axis. Data for the central part of M31 are shown with small empty circles, while data for the outer part are shown with blue circles. All PN densities were calculated within elliptical apertures in steps of 0.01 degrees for the central part and 0.2 degrees for the outer part. The final density distribution was normalized to have ~ 25 mag arcsec $^{-2}$ at a distance of 0.5° from the center. Fitting the data in the region $8 < R < 20$ kpc yields a scale length of 3.21 ± 0.14 kpc that is similar to the scale length 3.22 ± 0.02 kpc for the same region calculated by Ibata et al. (2007) using photometric data from the Isaac Newton Telescope Wide Field Camera survey of M31.

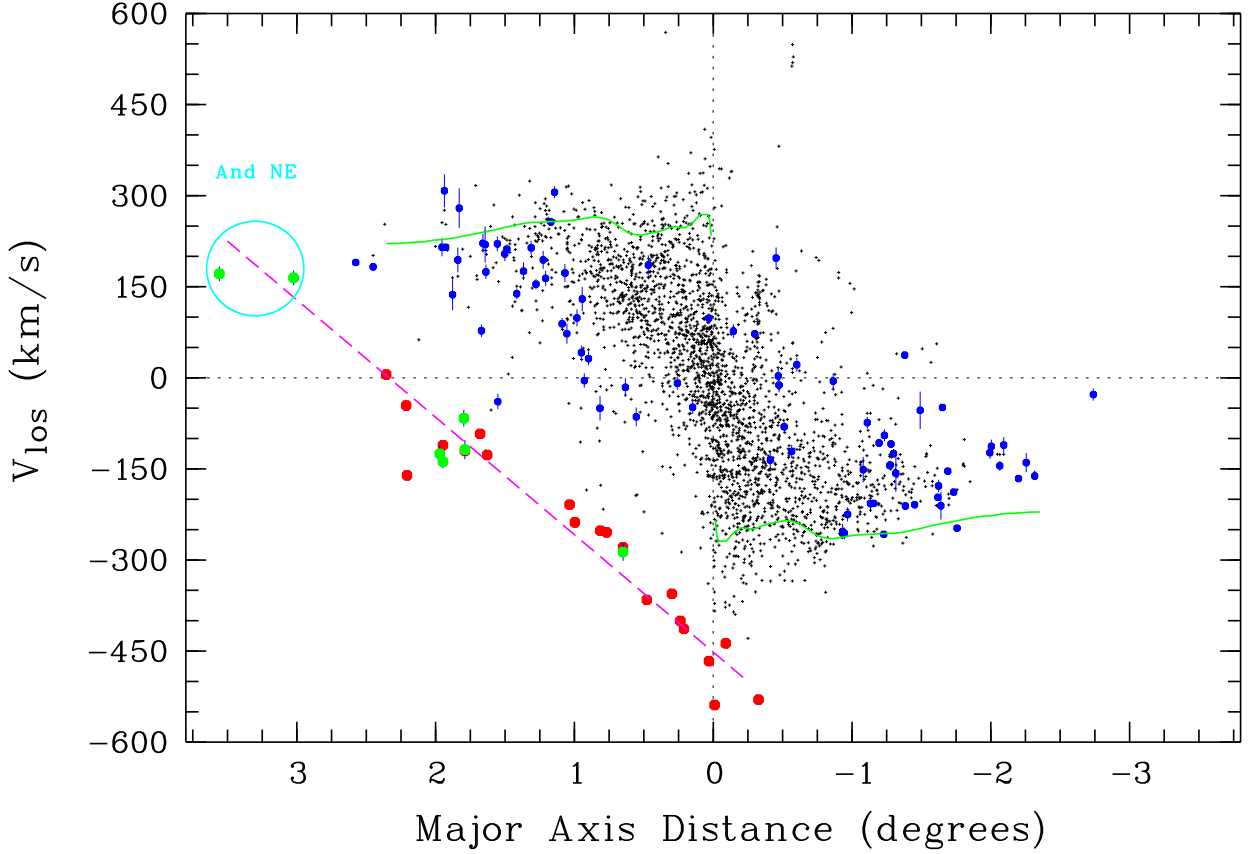


Fig. 16.— Velocity-distance diagram for newly discovered PNe in M31. All shown velocities of PNe are corrected for the systemic velocity $V_{\text{sys}} = -306 \text{ km s}^{-1}$ (Corbelli et al. 2010). X represents the projected distance along the major axis. The line is the HI rotation curve from Kent (1989). Black dots indicate PN data from M06 and HK04. Filled blue and green circles are newly observed PNe from our sample. The uncertainties of the velocity determination are shown by vertical error bars. Red filled circles mark PNe from M06, which were identified by M06 as forming a continuation of the Giant Stream. Green filled circles show those of our new PNe suggested to belong to the “continuation of the Giant Stream”. The position of PNe associated with Andromeda NE is also shown.

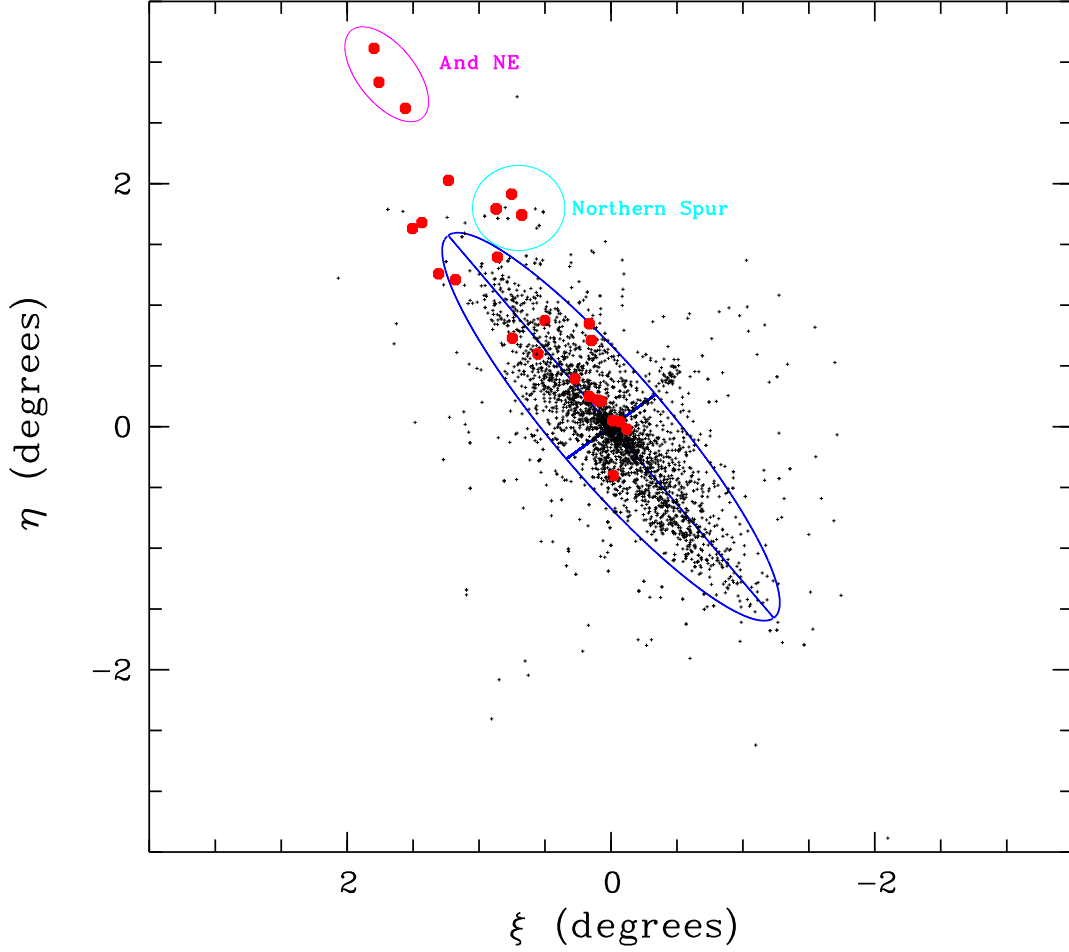


Fig. 17.— Positions of all PNe from HK04, M06, and our sample relative to the center and orientation of M31 (see caption of Figure 2 for more details). Red filled circles show PNe from M06 and our sample, which were identified as forming a continuation of the Giant Stream. The positions of the Northern Spur and Andromeda NE are shown.

Table 1. SDSS positions and magnitudes of selected PN candidates in SDSS M31 data

| # | SDSS name | $\alpha(2000.0)$ | $\delta(2000.0)$ | u_0 mag | g_0 mag | r_0 mag | i_0 mag | z_0 mag | pr ^a | obs ^b | Host ^c | sample ^d |
|----|----------------|------------------|------------------|--------------|--------------|--------------|--------------|--------------|-----------------|------------------|-------------------|---------------------|
| | (1) | (2) | (3) | (4) | (5) | (6) | (7) | (8) | (9) | (10) | (11) | (12) |
| 1 | J001934+351248 | 00:19:34.61 | +35:12:48.60 | 22.74±0.41 | 22.09±0.09 | 22.80±0.18 | 23.27±0.38 | 22.22±0.60 | 2 | 0 | | |
| 2 | J003206+375301 | 00:32:06.12 | +37:53:01.68 | 22.83±0.50 | 22.07±0.10 | 22.54±0.17 | 22.96±0.38 | 22.84±0.57 | 2 | 0 | | |
| 3 | J003338+395251 | 00:33:38.81 | +39:52:51.60 | 20.69±0.07 | 19.99±0.03 | 20.44±0.23 | 24.23±0.60 | 19.76±0.10 | 2 | 0 | | |
| 4 | J003351+402941 | 00:33:51.10 | +40:29:41.28 | 22.82±0.47 | 20.30±0.03 | 21.49±0.06 | 22.94±0.30 | 23.00±0.54 | 1 | 0 | SW | NF87 |
| 5 | J003419+404041 | 00:34:19.82 | +40:40:41.16 | 21.72±0.19 | 21.07±0.07 | 21.60±0.10 | 22.36±0.31 | 22.89±0.57 | 2 | 0 | | |
| 6 | J003447+393612 | 00:34:47.57 | +39:36:12.24 | 22.05±0.22 | 20.55±0.03 | 21.48±0.06 | 22.95±0.28 | 22.79±0.61 | 1 | 1 | G1 | |
| 7 | J003451+395429 | 00:34:51.19 | +39:54:29.16 | 22.29±0.37 | 20.64±0.04 | 21.44±0.08 | 23.02±0.45 | 22.30±0.66 | 1 | 1 | G1 | |
| 8 | J003451+402254 | 00:34:51.79 | +40:22:54.12 | 21.89±0.17 | 20.17±0.02 | 21.25±0.05 | 22.42±0.20 | 22.56±0.51 | 1 | 1 | SW | |
| 9 | J003509+392824 | 00:35:09.14 | +39:28:24.96 | 23.08±0.48 | 21.54±0.06 | 22.52±0.20 | 23.76±0.56 | 22.69±0.60 | 1 | 0 | G1 | NF87,M06 |
| 10 | J003533+405521 | 00:35:33.41 | +40:55:21.00 | 21.78±0.22 | 20.82±0.04 | 21.43±0.06 | 22.85±0.30 | 22.00±0.44 | 2 | 1 | SW | M06 |
| 11 | J003548+404039 | 00:35:48.98 | +40:40:39.00 | 23.12±0.72 | 21.64±0.06 | 22.06±0.16 | 22.73±0.60 | 22.77±0.83 | 2 | 0 | | |
| 12 | J003555+403126 | 00:35:55.70 | +40:31:26.04 | 24.28±0.74 | 21.30±0.05 | 22.28±0.11 | 23.15±0.36 | 23.60±0.38 | 1 | 0 | SW | NF87 |
| 13 | J003559+414050 | 00:35:59.83 | +41:40:50.52 | 22.95±0.58 | 21.83±0.07 | 22.58±0.20 | 23.20±0.52 | 22.40±0.65 | 2 | 1 | | |
| 14 | J003559+405033 | 00:35:59.98 | +40:50:33.36 | 22.27±0.38 | 21.09±0.04 | 21.82±0.11 | 22.81±0.46 | 22.18±1.19 | 1 | 0 | | NF87,M06 |
| 15 | J003600+392932 | 00:36:00.12 | +39:29:32.64 | 22.08±0.26 | 20.40±0.03 | 21.65±0.11 | 23.31±0.60 | 21.80±0.59 | 1 | 0 | GL | NF87 |
| 16 | J003605+403021 | 00:36:05.50 | +40:30:21.60 | 22.61±0.28 | 21.45±0.05 | 22.20±0.11 | 24.17±0.54 | 22.29±0.48 | 1 | 0 | SW | NF87 |
| 17 | J003612+393541 | 00:36:12.60 | +39:35:41.64 | 22.12±0.27 | 20.89±0.04 | 21.75±0.11 | 22.22±0.28 | 23.78±0.81 | 1 | 1 | GL | M06 |
| 18 | J003619+413807 | 00:36:19.08 | +41:38:07.44 | 20.44±0.07 | 19.84±0.02 | 20.25±0.14 | 24.22±0.75 | 19.32±0.07 | 2 | 0 | | |
| 19 | J003628+393526 | 00:36:28.78 | +39:35:26.16 | 22.62±0.40 | 20.19±0.03 | 21.27±0.07 | 22.87±0.38 | 23.49±0.60 | 1 | 1 | GL | M06 |
| 20 | J003634+395038 | 00:36:34.46 | +39:50:38.40 | 22.67±0.37 | 21.91±0.08 | 22.38±0.12 | 23.29±0.34 | 22.08±0.51 | 2 | 0 | | |
| 21 | J003635+401737 | 00:36:35.33 | +40:17:37.68 | 22.54±0.30 | 21.65±0.06 | 22.46±0.20 | 24.19±0.76 | 23.80±0.60 | 2 | 1 | | |
| 22 | J003644+400354 | 00:36:44.74 | +40:03:54.36 | 22.74±0.40 | 21.94±0.07 | 22.39±0.13 | 22.89±0.28 | 22.75±0.67 | 2 | 0 | | |
| 23 | J003653+401331 | 00:36:53.90 | +40:13:31.44 | 22.92±0.65 | 21.72±0.07 | 22.21±0.16 | 22.74±0.43 | 21.96±0.80 | 2 | 3 | | |
| 24 | J003654+395911 | 00:36:54.94 | +39:59:11.04 | 23.01±0.48 | 22.10±0.08 | 22.53±0.14 | 22.76±0.23 | 22.71±0.63 | 2 | 0 | | |
| 25 | J003657+395436 | 00:36:57.05 | +39:54:36.00 | 22.58±0.35 | 21.96±0.07 | 22.46±0.13 | 22.81±0.26 | 23.13±0.58 | 2 | 0 | | |
| 26 | J003703+394445 | 00:37:03.48 | +39:44:45.24 | 23.41±0.74 | 22.01±0.10 | 22.44±0.17 | 23.35±0.74 | 22.62±0.81 | 2 | 0 | | |

Table 1—Continued

| # | SDSS name | $\alpha(2000.0)$ | $\delta(2000.0)$ | u_0 mag | g_0 mag | r_0 mag | i_0 mag | z_0 mag | pr ^a | obs ^b | Host ^c | sample ^d |
|----|----------------|------------------|------------------|--------------|--------------|--------------|--------------|--------------|-----------------|------------------|-------------------|---------------------|
| | (1) | (2) | (3) | (4) | (5) | (6) | (7) | (8) | (9) | (10) | (11) | (12) |
| 27 | J003707+383856 | 00:37:07.13 | +38:38:56.76 | 22.26±0.27 | 21.25±0.04 | 22.25±0.12 | 23.29±0.34 | 21.82±0.35 | 1 | 1 | | |
| 28 | J003717+402437 | 00:37:17.30 | +40:24:37.80 | 23.09±0.79 | 20.69±0.03 | 21.31±0.08 | 22.57±0.33 | 22.62±0.87 | 1 | 1 | | |
| 29 | J003721+395050 | 00:37:21.12 | +39:50:50.64 | 22.54±0.38 | 20.73±0.04 | 21.51±0.08 | 22.81±0.42 | 22.25±0.79 | 1 | 0 | | NF87 |
| 30 | J003721+404142 | 00:37:21.82 | +40:41:42.72 | 22.80±0.39 | 21.81±0.07 | 22.69±0.16 | 23.24±0.39 | 22.86±0.49 | 2 | 1 | | M06 |
| 31 | J003726+401724 | 00:37:26.16 | +40:17:24.72 | 22.29±0.29 | 21.57±0.05 | 22.06±0.10 | 22.31±0.22 | 21.99±0.52 | 2 | 4 | | |
| 32 | J003734+402302 | 00:37:34.13 | +40:23:02.76 | 21.82±0.29 | 20.93±0.04 | 21.49±0.09 | 22.10±0.22 | 20.84±0.30 | 2 | 4 | | |
| 33 | J003736+402802 | 00:37:36.17 | +40:28:02.28 | 22.37±0.34 | 20.69±0.03 | 21.33±0.08 | 23.01±0.44 | 21.87±0.66 | 1 | 1 | | |
| 34 | J003736+394707 | 00:37:36.34 | +39:47:07.44 | 24.50±0.97 | 21.79±0.15 | 22.93±0.63 | 24.24±0.80 | 20.45±0.27 | 2 | 3 | | |
| 35 | J003736+393935 | 00:37:36.58 | +39:39:35.64 | 23.67±0.58 | 21.34±0.04 | 22.74±0.18 | 23.70±0.45 | 23.02±0.48 | 1 | 0 | | |
| 36 | J003738+395003 | 00:37:38.81 | +39:50:03.48 | 21.95±0.18 | 20.54±0.03 | 21.33±0.07 | 22.36±0.28 | 23.29±0.78 | 1 | 0 | | NF87 |
| 37 | J003739+393009 | 00:37:39.94 | +39:30:09.36 | 23.06±0.38 | 21.80±0.06 | 22.62±0.15 | 22.99±0.28 | 22.91±0.50 | 2 | 1 | GL | |
| 38 | J003742+395235 | 00:37:42.98 | +39:52:35.76 | 23.38±0.72 | 20.91±0.04 | 21.68±0.10 | 22.79±0.40 | 21.92±0.69 | 1 | 0 | | NF87 |
| 39 | J003745+403127 | 00:37:45.65 | +40:31:27.48 | 23.35±0.89 | 21.84±0.08 | 22.38±0.20 | 22.74±0.48 | 23.02±0.83 | 2 | 3 | | |
| 40 | J003749+405354 | 00:37:49.70 | +40:53:54.24 | 21.47±0.13 | 20.53±0.03 | 21.11±0.04 | 22.21±0.19 | 21.81±0.39 | 2 | 1 | | M06 |
| 41 | J003751+404547 | 00:37:51.29 | +40:45:47.88 | 22.19±0.35 | 20.42±0.03 | 21.16±0.07 | 22.72±0.39 | 23.69±0.54 | 1 | 1 | | M06 |
| 42 | J003808+395645 | 00:38:08.38 | +39:56:45.60 | 20.55±0.08 | 19.94±0.04 | 20.37±0.07 | 21.30±0.20 | 21.43±0.60 | 2 | 4 | | |
| 43 | J003818+400634 | 00:38:18.53 | +40:06:34.92 | 24.18±1.17 | 22.03±0.10 | 23.05±0.53 | 23.46±0.72 | 22.74±0.76 | 2 | 4 | | |
| 44 | J003818+421252 | 00:38:18.58 | +42:12:52.20 | 22.93±0.58 | 21.69±0.07 | 22.15±0.13 | 22.56±0.30 | 22.44±1.44 | 2 | 0 | | |
| 45 | J003827+404711 | 00:38:27.14 | +40:47:11.40 | 23.41±0.87 | 21.89±0.09 | 22.37±0.20 | 22.93±0.48 | 22.17±0.69 | 2 | 0 | | |
| 46 | J003832+401310 | 00:38:32.81 | +40:13:10.20 | 21.78±0.23 | 21.02±0.04 | 21.47±0.09 | 22.06±0.20 | 22.08±0.63 | 2 | 4 | | |
| 47 | J003841+394739 | 00:38:41.30 | +39:47:39.84 | 23.43±0.53 | 22.12±0.08 | 22.80±0.19 | 24.40±0.48 | 22.28±0.53 | 2 | 1 | GL | HK04 |
| 48 | J003846+412819 | 00:38:46.15 | +41:28:19.20 | 22.43±0.32 | 20.36±0.03 | 21.33±0.07 | 23.20±0.47 | 22.09±0.52 | 1 | 1 | LO | M06 |
| 49 | J003848+413937 | 00:38:48.38 | +41:39:37.44 | 23.02±0.49 | 22.19±0.10 | 22.89±0.26 | 23.94±0.70 | 21.66±0.42 | 2 | 1 | LO | M06 |
| 50 | J003849+400153 | 00:38:49.85 | +40:01:53.40 | 23.00±0.65 | 21.84±0.08 | 24.00±0.65 | 25.94±0.30 | 24.01±0.44 | 2 | 4 | | |
| 51 | J003849+400544 | 00:38:49.85 | +40:05:44.88 | 22.64±0.32 | 21.31±0.06 | 21.93±0.17 | 22.36±0.29 | 21.50±0.48 | 1 | 4 | | |
| 52 | J003852+404130 | 00:38:52.42 | +40:41:30.48 | 22.70±0.93 | 22.05±0.10 | 22.46±0.25 | 24.38±0.78 | 22.27±0.70 | 2 | 0 | | |

Table 1—Continued

| # | SDSS name | $\alpha(2000.0)$ | $\delta(2000.0)$ | u_0 mag | g_0 mag | r_0 mag | i_0 mag | z_0 mag | pr ^a | obs ^b | Host ^c | sample ^d |
|----|----------------|------------------|------------------|--------------|--------------|--------------|--------------|--------------|-----------------|------------------|-------------------|---------------------|
| | (1) | (2) | (3) | (4) | (5) | (6) | (7) | (8) | (9) | (10) | (11) | (12) |
| 53 | J003855+410655 | 00:38:55.03 | +41:06:55.08 | 22.80±0.40 | 20.54±0.03 | 21.73±0.08 | 22.47±0.24 | 22.30±0.47 | 1 | 1 | | M06 |
| 54 | J003901+415111 | 00:39:01.08 | +41:51:11.16 | 22.02±1.05 | 20.56±0.03 | 21.55±0.07 | 22.78±0.30 | 21.25±0.28 | 1 | 1 | LO | M06 |
| 55 | J003902+402250 | 00:39:02.52 | +40:22:50.16 | 23.46±0.91 | 20.75±0.04 | 21.76±0.13 | 25.14±0.60 | 21.88±0.60 | 1 | 1 | | HK04,M06 |
| 56 | J003903+394558 | 00:39:03.38 | +39:45:58.32 | 22.74±0.33 | 20.58±0.03 | 21.36±0.05 | 21.81±0.11 | 21.94±0.42 | 1 | 0 | GL | NF87,HK04 |
| 57 | J003903+395329 | 00:39:03.77 | +39:53:29.04 | 23.22±0.47 | 21.36±0.05 | 22.54±0.16 | 23.61±0.47 | 22.99±0.53 | 1 | 2 | | HK04 |
| 58 | J003906+401459 | 00:39:06.62 | +40:14:59.64 | 22.89±0.58 | 20.44±0.03 | 21.26±0.08 | 22.33±0.30 | 21.40±0.42 | 1 | 0 | | NF87,HK04,M06 |
| 59 | J003909+401120 | 00:39:09.31 | +40:11:20.76 | 23.74±1.26 | 20.55±0.03 | 21.39±0.09 | 22.02±0.24 | 22.20±0.72 | 1 | 0 | | NF87,HK04,M06 |
| 60 | J003915+404811 | 00:39:15.91 | +40:48:11.52 | 22.15±0.47 | 21.36±0.09 | 22.10±0.25 | 22.51±0.38 | 21.68±0.60 | 2 | 4 | | |
| 61 | J003916+402615 | 00:39:16.73 | +40:26:15.72 | 22.74±0.77 | 21.00±0.09 | 21.45±0.13 | 21.77±0.34 | 21.60±0.34 | 1 | 0 | | M06 |
| 62 | J003918+402126 | 00:39:18.07 | +40:21:26.64 | 21.38±0.22 | 20.59±0.04 | 21.05±0.08 | 21.52±0.18 | 22.27±0.71 | 2 | 4 | | |
| 63 | J003918+400919 | 00:39:18.55 | +40:09:19.80 | 21.96±0.27 | 20.58±0.03 | 22.20±0.18 | 22.52±0.55 | 23.29±0.68 | 1 | 0 | | NF87,M06,HK04 |
| 64 | J003922+410657 | 00:39:22.58 | +41:06:57.24 | 23.26±0.74 | 20.42±0.03 | 21.43±0.08 | 22.87±0.56 | 23.19±0.72 | 1 | 1 | | M06 |
| 65 | J003924+400702 | 00:39:24.53 | +40:07:02.28 | 22.50±0.29 | 20.58±0.03 | 21.62±0.07 | 23.69±0.46 | 22.33±1.44 | 1 | 0 | | NF87,HK04,M06 |
| 66 | J003929+405201 | 00:39:29.09 | +40:52:01.92 | 21.70±0.24 | 21.04±0.04 | 21.74±0.13 | 24.64±0.68 | 21.76±0.60 | 2 | 0 | | M06 |
| 67 | J003936+410608 | 00:39:36.17 | +41:06:08.64 | 22.67±0.96 | 21.65±0.07 | 22.18±0.16 | 22.39±0.27 | 22.36±0.76 | 2 | 0 | | |
| 68 | J003940+402554 | 00:39:40.44 | +40:25:54.84 | 22.06±0.37 | 20.99±0.06 | 21.45±0.12 | 22.71±0.36 | 22.02±0.58 | 1 | 4 | | |
| 69 | J003941+410145 | 00:39:41.81 | +41:01:45.84 | 22.83±0.56 | 22.04±0.10 | 22.55±0.26 | 23.09±0.38 | 22.32±0.75 | 2 | 0 | | |
| 70 | J003942+410221 | 00:39:42.53 | +41:02:21.12 | 23.13±1.11 | 21.51±0.06 | 22.44±0.21 | 24.03±0.74 | 22.52±0.78 | 1 | 0 | | M06 |
| 71 | J003945+403142 | 00:39:45.38 | +40:31:42.60 | 21.87±0.36 | 20.17±0.03 | 21.19±0.12 | 23.23±0.73 | 21.89±0.56 | 1 | 1 | | HK04,M06 |
| 72 | J003946+393842 | 00:39:46.70 | +39:38:42.72 | 21.81±0.24 | 21.13±0.04 | 21.64±0.10 | 23.87±0.73 | 21.97±0.66 | 2 | 0 | | HK04 |
| 73 | J003948+410841 | 00:39:48.19 | +41:08:41.64 | 22.67±0.53 | 20.92±0.12 | 21.72±0.21 | 23.33±0.71 | 22.08±0.38 | 1 | 0 | | |
| 74 | J003948+411043 | 00:39:48.77 | +41:10:43.32 | 22.75±0.52 | 21.19±0.05 | 22.30±0.18 | 23.83±0.68 | 21.76±0.57 | 1 | 1 | | |
| 75 | J003951+402327 | 00:39:51.86 | +40:23:27.96 | 20.59±0.13 | 19.85±0.03 | 20.26±0.04 | 20.51±0.08 | 20.77±0.26 | 2 | 4 | | |
| 76 | J003954+402338 | 00:39:54.17 | +40:23:38.40 | 21.43±0.26 | 20.22±0.03 | 21.14±0.12 | 21.51±0.31 | 20.72±0.25 | 1 | 4 | | |
| 77 | J003954+395103 | 00:39:54.38 | +39:51:03.24 | 23.04±0.82 | 21.05±0.04 | 22.55±0.19 | 24.09±0.70 | 21.92±0.57 | 1 | 0 | GL | NF87 |
| 78 | J003956+414306 | 00:39:56.88 | +41:43:06.96 | 24.01±0.85 | 21.59±0.07 | 23.06±0.31 | 23.33±0.55 | 23.04±0.63 | 1 | 0 | NGC205 | M06 |

Table 1—Continued

| # | SDSS name | $\alpha(2000.0)$ | $\delta(2000.0)$ | u_0 mag | g_0 mag | r_0 mag | i_0 mag | z_0 mag | pr ^a | obs ^b | Host ^c | sample ^d |
|-----|----------------|------------------|------------------|--------------|--------------|--------------|--------------|--------------|-----------------|------------------|-------------------|---------------------|
| | (1) | (2) | (3) | (4) | (5) | (6) | (7) | (8) | (9) | (10) | (11) | (12) |
| 79 | J003956+410507 | 00:39:56.98 | +41:05:07.44 | 21.95±0.29 | 20.41±0.03 | 21.08±0.07 | 23.04±0.35 | 22.84±0.78 | 1 | 1 | | M06 |
| 80 | J003958+402450 | 00:39:58.97 | +40:24:50.40 | 20.39±0.21 | 19.53±0.04 | 19.96±0.13 | 20.48±0.14 | 21.21±0.38 | 2 | 4 | | |
| 81 | J004000+410409 | 00:40:00.86 | +41:04:09.12 | 22.30±1.00 | 20.26±0.03 | 21.12±0.07 | 21.89±0.19 | 21.46±0.38 | 1 | 1 | | M06 |
| 82 | J004003+402721 | 00:40:03.02 | +40:27:21.60 | 20.84±0.15 | 19.60±0.02 | 20.03±0.04 | 20.28±0.08 | 20.51±0.20 | 2 | 4 | | |
| 83 | J004012+401302 | 00:40:12.79 | +40:13:02.28 | 22.97±0.44 | 21.36±0.05 | 22.92±0.22 | 24.08±0.49 | 22.48±0.50 | 1 | 0 | | HK04,M06 |
| 84 | J004013+401026 | 00:40:13.97 | +40:10:26.04 | 22.27±0.25 | 20.50±0.03 | 21.45±0.06 | 22.37±0.18 | 21.90±0.37 | 1 | 0 | | NF87,HK04 |
| 85 | J004035+421031 | 00:40:35.35 | +42:10:31.80 | 22.16±0.30 | 21.24±0.05 | 21.78±0.08 | 23.17±0.36 | 21.99±0.48 | 2 | 1 | LO | M06 |
| 86 | J004043+395705 | 00:40:43.54 | +39:57:05.40 | 22.79±0.66 | 21.11±0.04 | 22.22±0.17 | 25.49±0.43 | 23.66±0.76 | 1 | 0 | | NF87 |
| 87 | J004056+402008 | 00:40:56.88 | +40:20:08.88 | 21.98±0.20 | 20.12±0.02 | 21.23±0.05 | 22.32±0.27 | 21.54±0.33 | 1 | 1 | | HK04 |
| 88 | J004119+415146 | 00:41:19.08 | +41:51:46.44 | 22.97±0.43 | 22.01±0.08 | 22.76±0.19 | 24.19±0.56 | 23.41±0.44 | 2 | 2 | | M06 |
| 89 | J004133+412303 | 00:41:33.43 | +41:23:03.12 | 23.87±1.01 | 21.67±0.10 | 22.16±0.16 | 24.40±0.69 | 22.27±0.80 | 2 | 0 | | |
| 90 | J004133+412258 | 00:41:33.91 | +41:22:58.08 | 22.23±0.96 | 20.91±0.06 | 21.64±0.12 | 22.25±0.15 | 21.09±0.40 | 1 | 0 | | |
| 91 | J004138+395459 | 00:41:38.18 | +39:54:59.76 | 22.35±0.33 | 21.29±0.04 | 21.82±0.09 | 23.37±0.37 | 22.31±0.47 | 1 | 0 | | NF87,HK04,M06 |
| 92 | J004212+423134 | 00:42:12.43 | +42:31:34.32 | 22.75±0.53 | 21.54±0.06 | 22.74±0.19 | 23.11±0.40 | 22.96±0.56 | 1 | 1 | LO | |
| 93 | J004216+423826 | 00:42:16.51 | +42:38:26.16 | 24.68±0.96 | 22.03±0.09 | 22.44±0.16 | 22.98±0.38 | 23.46±0.47 | 2 | 0 | | |
| 94 | J004222+414313 | 00:42:22.15 | +41:43:13.08 | 23.23±0.76 | 21.90±0.09 | 22.85±0.28 | 24.21±0.70 | 22.41±0.84 | 2 | 0 | | |
| 95 | J004240+413548 | 00:42:40.61 | +41:35:48.48 | 22.13±1.09 | 20.31±0.05 | 21.30±0.13 | 24.24±0.63 | 23.52±0.54 | 1 | 0 | | M06 |
| 96 | J004244+401733 | 00:42:44.66 | +40:17:33.72 | 22.61±0.48 | 21.61±0.06 | 22.39±0.20 | 23.21±0.52 | 22.29±0.58 | 2 | 3 | | |
| 97 | J004252+402903 | 00:42:52.10 | +40:29:03.84 | 22.27±0.34 | 20.98±0.04 | 22.12±0.16 | 23.60±0.61 | 22.69±0.64 | 1 | 1 | | HK04,M06 |
| 98 | J004258+424732 | 00:42:58.46 | +42:47:32.64 | 22.18±0.33 | 21.09±0.04 | 21.72±0.09 | 23.63±0.56 | 22.68±0.57 | 1 | 1 | LO | |
| 99 | J004258+401140 | 00:42:58.90 | +40:11:40.20 | 22.15±0.27 | 21.53±0.05 | 21.94±0.10 | 22.54±0.23 | 21.94±0.42 | 2 | 0 | | |
| 100 | J004259+420213 | 00:42:59.09 | +42:02:13.92 | 22.32±1.02 | 20.55±0.03 | 21.46±0.06 | 22.75±0.34 | 22.86±0.53 | 1 | 1 | | M06 |
| 101 | J004303+401949 | 00:43:03.38 | +40:19:49.44 | 22.49±0.37 | 21.72±0.06 | 22.15±0.12 | 22.73±0.25 | 22.07±0.43 | 2 | 0 | | |
| 102 | J004306+404041 | 00:43:06.19 | +40:40:41.88 | 23.77±2.68 | 21.79±0.08 | 22.40±0.21 | 22.61±0.31 | 23.25±0.56 | 2 | 0 | | |
| 103 | J004311+422045 | 00:43:11.18 | +42:20:45.60 | 21.72±0.18 | 20.45±0.03 | 21.59±0.07 | 23.01±0.38 | 22.26±0.50 | 1 | 1 | | M06 |
| 104 | J004327+424203 | 00:43:27.24 | +42:42:03.60 | 22.28±0.33 | 21.12±0.05 | 22.15±0.14 | 22.85±0.47 | 21.80±0.47 | 1 | 1 | LO | |

Table 1—Continued

| # | SDSS name | $\alpha(2000.0)$ | $\delta(2000.0)$ | u_0 mag | g_0 mag | r_0 mag | i_0 mag | z_0 mag | pr ^a | obs ^b | Host ^c | sample ^d |
|-----|----------------|------------------|------------------|--------------|--------------|--------------|--------------|--------------|-----------------|------------------|-------------------|---------------------|
| | (1) | (2) | (3) | (4) | (5) | (6) | (7) | (8) | (9) | (10) | (11) | (12) |
| 105 | J004328+415155 | 00:43:28.46 | +41:51:55.44 | 23.60±1.07 | 21.69±0.09 | 22.33±0.19 | 22.55±0.48 | 23.51±0.66 | 2 | 0 | | M06 |
| 106 | J004332+415842 | 00:43:32.35 | +41:58:42.24 | 21.84±0.27 | 20.57±0.03 | 21.19±0.06 | 22.06±0.21 | 21.99±0.78 | 1 | 1 | GS | M06 |
| 107 | J004336+414942 | 00:43:36.58 | +41:49:42.96 | 21.86±0.49 | 20.26±0.04 | 21.25±0.09 | 22.38±0.45 | 22.05±0.89 | 1 | 0 | | M06 |
| 108 | J004342+422235 | 00:43:42.53 | +42:22:35.40 | 22.81±0.38 | 20.80±0.04 | 21.83±0.10 | 22.70±0.33 | 22.05±0.35 | 1 | 1 | | M06 |
| 109 | J004352+421835 | 00:43:52.22 | +42:18:35.28 | 22.48±0.34 | 21.62±0.06 | 22.04±0.11 | 22.32±0.22 | 22.54±0.53 | 2 | 0 | | |
| 110 | J004402+421716 | 00:44:02.35 | +42:17:16.44 | 22.73±0.41 | 20.51±0.03 | 21.46±0.06 | 22.51±0.25 | 22.65±0.53 | 1 | 1 | | M06 |
| 111 | J004403+422746 | 00:44:03.12 | +42:27:46.44 | 22.57±0.36 | 20.41±0.03 | 21.37±0.06 | 22.74±0.32 | 21.63±0.47 | 1 | 1 | | |
| 112 | J004410+412420 | 00:44:10.61 | +41:24:20.16 | 20.79±0.41 | 19.41±0.05 | 20.71±0.12 | 21.16±0.20 | 20.19±0.26 | 2 | 4 | | M06 |
| 113 | J004421+422450 | 00:44:21.50 | +42:24:50.04 | 22.70±0.64 | 20.90±0.04 | 22.06±0.11 | 23.48±0.55 | 21.88±0.42 | 1 | 2 | | M06 |
| 114 | J004430+420857 | 00:44:30.74 | +42:08:57.48 | 23.41±0.92 | 22.19±0.11 | 22.86±0.26 | 25.11±0.51 | 23.23±0.79 | 2 | 4 | | M06 |
| 115 | J004450+420506 | 00:44:50.86 | +42:05:06.36 | 23.46±0.97 | 21.57±0.07 | 21.97±0.13 | 23.05±0.37 | 22.66±0.70 | 1 | 0 | | M06 |
| 116 | J004452+421316 | 00:44:52.92 | +42:13:16.68 | 22.22±0.38 | 21.39±0.05 | 21.90±0.12 | 22.13±0.22 | 21.89±0.65 | 2 | 4 | | |
| 117 | J004454+421738 | 00:44:54.77 | +42:17:38.04 | 23.07±0.73 | 21.41±0.05 | 22.36±0.17 | 24.81±0.64 | 22.73±0.82 | 1 | 1 | | |
| 118 | J004501+421423 | 00:45:01.49 | +42:14:23.64 | 21.24±0.17 | 20.64±0.05 | 21.07±0.12 | 21.33±0.23 | 20.73±0.34 | 2 | 4 | | |
| 119 | J004523+421521 | 00:45:23.18 | +42:15:21.96 | 22.76±0.56 | 21.95±0.09 | 22.86±0.31 | 24.34±0.76 | 22.60±0.81 | 2 | 4 | | |
| 120 | J004537+422430 | 00:45:37.70 | +42:24:30.60 | 24.86±0.92 | 21.99±0.08 | 22.68±0.32 | 24.80±0.69 | 22.64±0.81 | 2 | 4 | | |
| 121 | J004542+425526 | 00:45:42.60 | +42:55:26.04 | 22.05±0.23 | 20.46±0.03 | 21.26±0.06 | 21.64±0.12 | 21.14±0.24 | 1 | 1 | SP | NF87,M06 |
| 122 | J004544+422912 | 00:45:44.35 | +42:29:12.12 | 23.15±0.70 | 22.20±0.10 | 22.66±0.45 | 24.78±0.70 | 23.67±0.56 | 2 | 4 | | |
| 123 | J004552+423652 | 00:45:52.80 | +42:36:52.92 | 21.93±0.29 | 20.36±0.03 | 21.10±0.06 | 22.56±0.42 | 23.82±0.51 | 1 | 1 | | NF87,M06 |
| 124 | J004613+424028 | 00:46:13.82 | +42:40:28.56 | 21.76±0.22 | 20.59±0.03 | 21.52±0.09 | 23.17±0.49 | 23.44±0.65 | 1 | 1 | | NF87,M06 |
| 125 | J004619+412230 | 00:46:19.92 | +41:22:30.36 | 21.42±0.19 | 20.81±0.04 | 21.22±0.07 | 21.72±0.14 | 21.74±0.51 | 2 | 0 | | |
| 126 | J004626+430043 | 00:46:26.50 | +43:00:43.20 | 21.92±0.21 | 20.18±0.02 | 21.07±0.05 | 22.04±0.16 | 21.77±0.37 | 1 | 1 | GS | NF87,M06 |
| 127 | J004641+435903 | 00:46:41.62 | +43:59:03.48 | 23.96±1.08 | 21.54±0.06 | 22.51±0.18 | 23.13±0.52 | 22.01±0.52 | 1 | 0 | | JF86 |
| 128 | J004642+420835 | 00:46:42.94 | +42:08:35.52 | 21.71±0.29 | 19.98±0.03 | 20.99±0.07 | 21.92±0.34 | 22.08±0.62 | 1 | 1 | | M06 |
| 129 | J004648+412352 | 00:46:48.07 | +41:23:52.80 | 22.59±0.50 | 21.91±0.10 | 22.52±0.20 | 23.78±0.63 | 22.49±0.73 | 2 | 0 | | |
| 130 | J004652+431058 | 00:46:52.15 | +43:10:58.80 | 22.64±0.37 | 20.96±0.04 | 22.10±0.11 | 23.86±0.59 | 22.34±0.50 | 1 | 1 | GS | |

Table 1—Continued

| # | SDSS name | $\alpha(2000.0)$ | $\delta(2000.0)$ | u_0 mag | g_0 mag | r_0 mag | i_0 mag | z_0 mag | pr ^a | obs ^b | Host ^c | sample ^d |
|-----|----------------|------------------|------------------|--------------|--------------|--------------|--------------|--------------|-----------------|------------------|-------------------|---------------------|
| | (1) | (2) | (3) | (4) | (5) | (6) | (7) | (8) | (9) | (10) | (11) | (12) |
| 131 | J004655+422401 | 00:46:55.46 | +42:24:01.80 | 21.65±0.21 | 19.99±0.02 | 21.01±0.05 | 21.55±0.11 | 20.39±0.17 | 1 | 1 | | M06 |
| 132 | J004659+423758 | 00:46:59.28 | +42:37:58.08 | 22.18±0.32 | 20.51±0.03 | 21.33±0.08 | 22.92±0.42 | 22.88±0.79 | 1 | 1 | | NF87,M06 |
| 133 | J004700+425855 | 00:47:00.77 | +42:58:55.20 | 21.76±0.19 | 20.25±0.03 | 21.26±0.05 | 22.26±0.19 | 22.57±0.51 | 1 | 1 | SP | NF87,M06 |
| 134 | J004700+404923 | 00:47:00.98 | +40:49:23.16 | 23.30±0.60 | 21.50±0.07 | 22.34±0.16 | 24.62±0.67 | 21.65±0.43 | 1 | 1 | NS | HK04,M06 |
| 135 | J004706+420715 | 00:47:06.36 | +42:07:15.24 | 21.52±0.21 | 20.31±0.03 | 21.56±0.11 | 24.31±0.74 | 21.74±0.44 | 1 | 1 | | M06 |
| 136 | J004711+423047 | 00:47:11.93 | +42:30:47.16 | 23.01±0.58 | 20.94±0.04 | 21.65±0.09 | 23.34±0.55 | 22.64±0.72 | 1 | 1 | | NF87,M06 |
| 137 | J004725+425859 | 00:47:25.90 | +42:58:59.88 | 23.37±0.78 | 20.97±0.04 | 21.87±0.11 | 23.01±0.41 | 22.96±0.83 | 1 | 1 | SP | M06 |
| 138 | J004730+430341 | 00:47:30.34 | +43:03:41.04 | 23.18±0.57 | 20.41±0.03 | 21.55±0.09 | 22.92±0.44 | 22.31±0.51 | 1 | 1 | GS | M06 |
| 139 | J004731+422618 | 00:47:31.58 | +42:26:18.24 | 23.17±0.76 | 21.50±0.06 | 22.35±0.16 | 22.71±0.32 | 23.03±0.67 | 1 | 0 | | M06 |
| 140 | J004732+421135 | 00:47:32.93 | +42:11:35.88 | 22.00±0.28 | 20.43±0.03 | 21.08±0.06 | 21.57±0.16 | 23.03±0.64 | 1 | 1 | | M06 |
| 141 | J004734+420408 | 00:47:34.15 | +42:04:08.04 | 22.50±0.44 | 20.88±0.04 | 21.49±0.09 | 22.95±0.48 | 23.07±0.65 | 1 | 4 | | M06 |
| 142 | J004746+421214 | 00:47:46.75 | +42:12:14.76 | 21.92±0.25 | 20.40±0.03 | 21.71±0.11 | 22.50±0.35 | 22.56±0.68 | 1 | 1 | | M06 |
| 143 | J004753+421457 | 00:47:53.59 | +42:14:57.48 | 22.26±0.38 | 21.06±0.04 | 22.05±0.15 | 22.89±0.44 | 23.76±0.83 | 1 | 0 | | M06 |
| 144 | J004757+412810 | 00:47:57.38 | +41:28:10.56 | 23.83±1.01 | 22.17±0.10 | 22.58±0.24 | 22.84±0.36 | 22.32±0.56 | 2 | 0 | | M06 |
| 145 | J004758+430006 | 00:47:58.61 | +43:00:06.48 | 21.94±0.26 | 20.56±0.03 | 21.21±0.19 | 22.88±0.48 | 22.80±0.86 | 1 | 1 | SP | NF87,M06 |
| 146 | J004801+414410 | 00:48:01.20 | +41:44:10.68 | 23.21±0.84 | 22.03±0.19 | 22.54±0.50 | 24.20±0.68 | 21.06±0.41 | 2 | 3 | | M06 |
| 147 | J004803+423637 | 00:48:03.53 | +42:36:37.80 | 21.97±0.24 | 20.70±0.03 | 21.40±0.06 | 22.37±0.20 | 22.39±0.65 | 1 | 1 | | NF87,M06 |
| 148 | J004804+423510 | 00:48:04.90 | +42:35:10.68 | 23.16±0.65 | 21.79±0.06 | 22.88±0.22 | 24.33±0.53 | 23.62±0.50 | 2 | 1 | | M06 |
| 149 | J004811+414453 | 00:48:11.02 | +41:44:53.88 | 22.13±0.35 | 21.46±0.05 | 21.86±0.11 | 22.27±0.26 | 21.52±0.42 | 2 | 0 | | M06 |
| 150 | J004822+404541 | 00:48:22.15 | +40:45:41.40 | 22.18±0.21 | 21.02±0.04 | 21.68±0.08 | 23.29±0.42 | 22.99±0.52 | 1 | 1 | NS | HK04,M06 |
| 151 | J004824+410811 | 00:48:24.79 | +41:08:11.04 | 21.76±0.20 | 19.80±0.03 | 21.00±0.05 | 22.25±0.23 | 22.26±0.68 | 2 | 1 | NS | HK04 |
| 152 | J004830+414700 | 00:48:30.41 | +41:47:00.96 | 23.27±0.82 | 21.06±0.04 | 22.52±0.20 | 24.30±0.69 | 21.86±0.51 | 1 | 1 | | M06 |
| 153 | J004847+425136 | 00:48:47.90 | +42:51:36.00 | 22.11±0.28 | 20.34±0.02 | 20.92±0.04 | 22.17±0.17 | 21.01±0.27 | 1 | 1 | | M06 |
| 154 | J004854+424953 | 00:48:54.05 | +42:49:53.76 | 22.49±0.38 | 21.00±0.04 | 21.92±0.09 | 22.50±0.22 | 23.25±0.58 | 1 | 0 | | NF87,M06 |
| 155 | J004901+415245 | 00:49:01.10 | +41:52:45.48 | 22.12±0.32 | 21.25±0.05 | 21.69±0.10 | 22.10±0.30 | 22.33±0.57 | 2 | 0 | | M06 |
| 156 | J004915+412046 | 00:49:15.70 | +41:20:46.68 | 22.34±0.30 | 20.13±0.02 | 21.45±0.07 | 22.24±0.24 | 23.20±0.69 | 1 | 1 | NS | M06 |

Table 1—Continued

| # | SDSS name | $\alpha(2000.0)$ | $\delta(2000.0)$ | u_0 mag | g_0 mag | r_0 mag | i_0 mag | z_0 mag | pr ^a | obs ^b | Host ^c | sample ^d |
|-----|----------------|------------------|------------------|--------------|--------------|--------------|--------------|--------------|-----------------|------------------|-------------------|---------------------|
| | (1) | (2) | (3) | (4) | (5) | (6) | (7) | (8) | (9) | (10) | (11) | (12) |
| 157 | J004931+423737 | 00:49:31.94 | +42:37:37.92 | 22.38±0.25 | 20.72±0.03 | 21.58±0.09 | 22.53±0.28 | 23.44±0.56 | 1 | 1 | | M06 |
| 158 | J004949+423139 | 00:49:49.82 | +42:31:39.72 | 23.10±0.51 | 21.19±0.04 | 21.93±0.10 | 22.94±0.28 | 22.25±0.42 | 1 | 1 | GS | |
| 159 | J005038+411815 | 00:50:38.66 | +41:18:15.84 | 22.55±0.42 | 20.66±0.03 | 21.76±0.08 | 23.19±0.41 | 22.29±0.92 | 1 | 1 | NS | |
| 160 | J005123+435321 | 00:51:23.45 | +43:53:21.84 | 22.36±0.30 | 20.80±0.03 | 21.83±0.09 | 22.87±0.32 | 22.43±0.48 | 1 | 1 | NE | |
| 161 | J005130+420657 | 00:51:30.62 | +42:06:57.96 | 22.93±0.52 | 21.08±0.04 | 21.78±0.09 | 22.66±0.24 | 21.71±0.43 | 1 | 1 | NS | |
| 162 | J005134+415704 | 00:51:34.99 | +41:57:04.68 | 23.55±0.65 | 21.24±0.07 | 21.75±0.11 | 23.58±0.68 | 22.32±0.63 | 1 | 1 | NS | |
| 163 | J005200+430323 | 00:52:00.12 | +43:03:23.76 | 22.70±0.39 | 21.41±0.05 | 22.08±0.12 | 24.04±0.65 | 22.46±0.60 | 1 | 0 | | NF87,M06 |
| 164 | J005232+440613 | 00:52:32.04 | +44:06:13.32 | 23.21±0.70 | 21.26±0.04 | 21.75±0.09 | 23.00±0.38 | 22.23±1.55 | 1 | 0 | NE | |
| 165 | J005247+442257 | 00:52:47.50 | +44:22:57.72 | 21.95±0.24 | 21.02±0.04 | 21.82±0.09 | 22.79±0.31 | 22.02±1.49 | 2 | 1 | NE | |
| 166 | J005357+422928 | 00:53:57.19 | +42:29:28.32 | 25.16±0.63 | 20.11±0.02 | 24.22±0.58 | 24.49±0.67 | 19.63±0.07 | 1 | 0 | | |
| 167 | J010956+482118 | 01:09:56.42 | +48:21:18.72 | 22.67±1.26 | 20.93±0.07 | 21.41±0.13 | 21.91±0.29 | 20.90±0.33 | 1 | 0 | | |

^a1 – first priority candidate; 2 – second priority candidate

^b0 – not observed; 1 – confirmed PN; 2 – not detected in our follow-up, but identified later via cross-identifications with other catalogs; 3 – not detected in our follow-up; 4 – our unobserved candidates with obvious emission in [O III] λ 5007 and H α narrow filters from SLGG data

^cSW – SW Shell; G1 – G1 Clump; GL – G1 Clump loop; LO – NGC 205 Loop; NGC205 – in NGC 205; SP – Northern Spur; GS – Giant Stream; NS – NE Shelf; NE – Andromeda NE

^dCross-identification from other catalogues: JF86 – Jacoby & Ford (1986); NF87 – Nolthenius & Ford (1987); HK04 – Hurley-Keller et al. (2004); M06 – Merrett et al. (2006).

Table 2. Heliocentric velocities and observed line fluxes of our confirmed PNe in M31

| # | SDSS name | V \pm dV km/s | F(H β) ^a | F(5007) ^a | F(H α) ^a | F(6584) ^a | C(H β) |
|----|----------------|--------------------|----------------------------|----------------------|-----------------------------|----------------------|---------------|
| | (1) | (2) | (3) | (4) | (5) | (6) | (7) |
| 1 | J003447+393612 | −440 \pm 16 | 6.2 | 89.5 | 27.5 | 3.2 | 0.56 |
| 2 | J003451+395429 | −413 \pm 11 | 5.4 | 77.4 | 17.9 | 6.5 | 0.17 |
| 3 | J003451+402254 | −478 \pm 10 | ... | 132.0 | 27.1 | 5.6 | ... |
| 4 | J003533+405521 | −374 \pm 10 | 15.8 | 99.4 | 47.5 | 5.2 | 0.08 |
| 5 | J003559+414050 | −103 \pm 17 | ... | 27.9 | 10.4 | ... | ... |
| 6 | J003612+393541 | −411 \pm 13 | 10.7 | 120.2 | 36.2 | ... | 0.21 |
| 7 | J003628+393526 | −445 \pm 8 | 21.5 | 368.8 | 68.6 | 8.1 | 0.11 |
| 8 | J003635+401737 | −354 \pm 31 | ... | 28.6 | 7.1 | ... | ... |
| 9 | J003707+383856 | −327 \pm 10 | ... | 107.1 | 24.1 | ... | ... |
| 10 | J003717+402437 | −457 \pm 31 | 4.0 | 60.2 | 16.6 | 4.5 | 0.47 |
| 11 | J003721+404142 | −451 \pm 21 | ... | 22.7 | 5.8 | ... | ... |
| 12 | J003736+402802 | −395 \pm 10 | 10.5 | 116.4 | 36.5 | 5.0 | 0.24 |
| 13 | J003739+393009 | −423 \pm 10 | 4.5 | 49.3 | 16.4 | ... | 0.30 |
| 14 | J003749+405354 | −305 \pm 13 | 15.6 | 146.6 | 65.3 | 8.2 | 0.50 |
| 15 | J003751+404547 | −525 \pm 12 | 18.4 | 185.2 | 71.5 | ... | 0.40 |
| 16 | J003841+394739 | −511 \pm 23 | 3.0 | 31.2 | 11.9 | ... | 0.42 |
| 17 | J003846+412819 | −228 \pm 6 | 7.7 | 93.8 | 32.1 | ... | 0.48 |
| 18 | J003848+413937 | −223 \pm 11 | 4.8 | 52.9 | 16.4 | 2.8 | 0.22 |
| 19 | J003855+410655 | −421 \pm 11 | ... | 82.2 | 16.6 | ... | ... |
| 20 | J003901+415111 | −202 \pm 8 | 16.3 | 143.7 | 51.2 | ... | 0.12 |
| 21 | J003902+402250 | −507 \pm 12 | 6.4 | 76.6 | 19.8 | 3.8 | 0.09 |
| 22 | J003922+410657 | −381 \pm 8 | 12.1 | 187.1 | 41.7 | 11.1 | 0.22 |
| 23 | J003945+403142 | −553 \pm 12 | 10.9 | 200.0 | 38.5 | 16.5 | 0.24 |
| 24 | J003948+411043 | −435 \pm 14 | 3.1 | 49.2 | 12.7 | ... | 0.45 |
| 25 | J003956+410507 | −297 \pm 15 | 9.2 | 100.6 | 33.4 | 10.5 | 0.29 |
| 26 | J004000+410409 | −312 \pm 12 | ... | 149.5 | 29.1 | ... | ... |
| 27 | J004035+421031 | −114 \pm 16 | 6.1 | 42.0 | 19.0 | 4.3 | 0.14 |
| 28 | J004056+402008 | −556 \pm 10 | 8.7 | 143.0 | 27.8 | 6.5 | 0.11 |
| 29 | J004212+423134 | −305 \pm 12 | 4.4 | 58.3 | 15.0 | 3.3 | 0.22 |

Table 2—Continued

| # | SDSS name | V±dV km/s | F(H β) ^a | F(5007) ^a | F(H α) ^a | F(6584) ^a | C(H β) |
|----|----------------|--------------|----------------------------|----------------------|-----------------------------|----------------------|---------------|
| | (1) | (2) | (3) | (4) | (5) | (6) | (7) |
| 30 | J004252+402903 | −278±11 | 4.0 | 71.4 | 14.8 | 5.2 | 0.29 |
| 31 | J004258+424732 | −106±15 | 6.3 | 46.5 | 26.7 | ... | 0.51 |
| 32 | J004259+420213 | −316±15 | 4.4 | 42.2 | 16.1 | ... | 0.34 |
| 33 | J004311+422045 | −268±11 | ... | 92.7 | 22.3 | ... | ... |
| 34 | J004327+424203 | −136±12 | 10.1 | 118.6 | 35.3 | ... | 0.25 |
| 35 | J004332+415842 | −587±15 | 6.4 | 92.8 | 32.4 | 8.3 | 0.72 |
| 36 | J004342+422235 | −201±14 | 4.0 | 59.7 | 14.8 | 2.7 | 0.31 |
| 37 | J004402+421716 | −259±12 | 8.4 | 115.6 | 34.6 | 6.6 | 0.46 |
| 38 | J004403+422746 | −211±10 | 12.0 | 144.4 | 41.5 | 7.6 | 0.24 |
| 39 | J004454+421738 | −227±17 | 5.4 | 54.9 | 17.8 | 5.4 | 0.17 |
| 40 | J004542+425526 | −126±12 | 11.9 | 179.5 | 39.5 | 8.4 | 0.17 |
| 41 | J004552+423652 | −162±9 | 18.4 | 181.3 | 57.8 | 11.4 | 0.12 |
| 42 | J004613+424028 | −96±12 | 8.0 | 101.9 | 23.7 | ... | 0.03 |
| 43 | J004626+430043 | −418±16 | 14.6 | 225.4 | 47.2 | 16.7 | 0.14 |
| 44 | J004642+420835 | 6±10 | 15.7 | 308.9 | 48.2 | 9.6 | 0.05 |
| 45 | J004652+431058 | −425±14 | 7.5 | 133.8 | 26.3 | 5.1 | 0.22 |
| 46 | J004655+422401 | −124±15 | 12.1 | 238.3 | 53.9 | 14.7 | 0.54 |
| 47 | J004659+423758 | −79±12 | 11.5 | 100.5 | 33.8 | 12.5 | 0.05 |
| 48 | J004700+425855 | −21±33 | 7.2 | 137.6 | 31.0 | ... | 0.49 |
| 49 | J004700+404923 | −348±11 | 5.0 | 59.1 | 17.4 | 6.9 | 0.25 |
| 50 | J004706+420715 | −43±6 | 14.1 | 227.4 | 42.3 | 9.1 | 0.04 |
| 51 | J004711+423047 | −88±8 | 9.1 | 93.1 | 29.2 | 12.5 | 0.16 |
| 52 | J004725+425859 | −163±26 | ... | 63.9 | 22.3 | ... | ... |
| 53 | J004730+430341 | −438±11 | 8.5 | 93.2 | 29.0 | ... | 0.22 |
| 54 | J004732+421135 | −146±8 | 8.9 | 105.4 | 35.3 | 8.5 | 0.41 |
| 55 | J004746+421214 | −86±12 | ... | 105.4 | 33.4 | ... | ... |
| 56 | J004758+430006 | −85±15 | 8.5 | 48.0 | 28.1 | ... | 0.22 |
| 57 | J004803+423637 | −78±15 | 6.5 | 70.6 | 29.3 | ... | 0.58 |
| 58 | J004804+423510 | −80±30 | ... | 12.6 | 6.8 | ... | ... |

Table 2—Continued

| # | SDSS name | V±dV km/s | F(H β) ^a | F(5007) ^a | F(H α) ^a | F(6584) ^a | C(H β) |
|----|----------------|--------------|----------------------------|----------------------|-----------------------------|----------------------|---------------|
| | (1) | (2) | (3) | (4) | (5) | (6) | (7) |
| 59 | J004822+404541 | −309±11 | 6.1 | 50.2 | 19.2 | ... | 0.14 |
| 60 | J004824+410811 | −364±15 | 21.5 | 362.4 | 84.6 | 13.9 | 0.38 |
| 61 | J004830+414700 | −127±15 | 3.3 | 75.7 | 12.9 | ... | 0.34 |
| 62 | J004847+425136 | 8±27 | ... | 122.2 | 39.3 | ... | ... |
| 63 | J004915+412046 | −350±20 | 13.5 | 207.7 | 48.8 | 5.9 | 0.28 |
| 64 | J004931+423737 | −106±20 | 10.5 | 133.8 | 33.5 | ... | 0.12 |
| 65 | J004949+423139 | −367±14 | 4.5 | 69.6 | 19.1 | ... | 0.48 |
| 66 | J005038+411815 | −170±20 | 6.3 | 104.9 | 20.7 | ... | 0.14 |
| 67 | J005123+435321 | −135±12 | 7.3 | 108.5 | 24.2 | 7.1 | 0.17 |
| 68 | J005130+420657 | −222±10 | 9.0 | 111.8 | 35.0 | 11.4 | 0.38 |
| 69 | J005134+415704 | −339±13 | 7.2 | 75.5 | 22.1 | 7.2 | 0.09 |
| 70 | J005247+442257 | −129±12 | 6.1 | 66.6 | 20.5 | 4.5 | 0.20 |

^aObserved flux in units of 10^{-16} ergs s^{−1}cm^{−2}